

THE MASS-METALLICITY AND LUMINOSITY-METALLICITY RELATION FROM DEEP2 AT $z \sim 0.8$

H. JABRAN ZAHID, LISA J. KEWLEY, FABIO BRESOLIN
 Institute for Astronomy 2680 Woodlawn Dr., Honolulu, HI 96822
Submitted to ApJ April 28, 2010

ABSTRACT

In this paper, we present results from our study investigating the evolution of the mass-metallicity and luminosity-metallicity relation over cosmological timescales. We determine the metallicities from strong-line diagnostics for 940 emission line galaxies from the Deep Extragalactic Evolutionary Probe 2 (DEEP2) redshift survey in the redshift range of $0.75 < z < 0.82$. We determine masses by fitting the SED inferred from photometry with stellar population synthesis models. This relatively large sample of galaxies in a small redshift range is ideal for investigating metallicity evolution in comparison with local and high- z samples. This work increases the number of galaxies with determined metallicities in this redshift range by an order of magnitude. We investigate the evolution in the mass-metallicity and luminosity-metallicity relation by comparing our determination at $z \sim 0.8$ with the local relation at $z \sim 0.07$ determined from the Sloan Digital Sky Survey (SDSS). We show that at $z \sim 0.8$ galaxies with masses $M \gtrsim 10^{10.5} M_{\odot}$ have already achieved the level of enrichment observed in the local universe. The mass-metallicity relation for $z \sim 0.8$ has slightly steeper slope than the local relation and the mean difference in metallicity is ~ 0.05 dex. We examine the luminosity-metallicity relation and determine that the slope of the relation at $z \sim 0.8$ is consistent with the local relation. The metallicity at a given luminosity in the $z \sim 0.8$ is offset from the local relation by ~ 0.12 dex. We attribute the discrepancy between the metallicity evolution inferred from the mass-metallicity and luminosity-metallicity relation to luminosity evolution in the population of blue star-forming galaxies. We infer a B-band luminosity evolution of ~ 0.8 mags for the population of star-forming galaxies. We estimate gas masses from the Schmidt-Kennicutt star formation law and determine the effective yields for our sample. We observe an effective yield that decreases with increasing stellar mass and we discuss the implications of this result.

Subject headings:

1. INTRODUCTION

The heavy-element abundance in galaxies is a key physical property for understanding galaxy evolution. Metals are formed in massive stars and are dispersed into the interstellar medium (ISM) via mass-loss processes. Metallicity, therefore, provides an important record of the star formation history of a galaxy. Galaxies and their chemical abundances, however, do not evolve as closed systems where metals are dispersed into the ISM as gas is converted into stars. Rather, they are modulated by inflow of unenriched gas and a complex "feedback" mechanism where supernovae and stellar winds influence the ISM by inducing outflows of gas into the intergalactic medium (IGM) and regulating star formation through reheating (Larson 1974; Larson & Dinerstein 1975; Kauffmann & Charlot 1998; Somerville & Primack 1999; Springel & Hernquist 2003).

A simple "closed-box" model in which feedback is not considered predicts a correlation between two fundamental parameters—mass and metallicity (van den Bergh 1962; Schmidt 1963; Searle & Sargent 1972; Erb et al. 2006). The pioneering work of Lequeux et al. (1979) first showed this correlation in local irregular galaxies. Many subsequent efforts have focused on the relation between luminosity and metallicity (Skillman et al. 1989; Zaritsky et al. 1994; Garnett et al. 1997; Lamareille et al. 2004; Salzer et al. 2005) where luminosity is taken as a proxy for mass because of the difficulty in inferring galaxy masses from observables. Early attempts to ex-

tend this relation to intermediate redshifts found that the luminosity-metallicity (LZ) relation at earlier epochs was consistent with the local universe (Kobulnicky et al. 1999; Carollo & Lilly 2001). However, many recent investigations have provided compelling evidence for evolution of the LZ relation over cosmological times (Kobulnicky & Koo 2000; Pettini et al. 2001; Kobulnicky et al. 2003; Kobulnicky & Kewley 2004; Maier et al. 2004; Shapley et al. 2004, 2005). Luminosities of galaxies evolve along with their chemical abundances on cosmological timescales and disentangling the contribution for each has posed difficulties in these studies.

Evolution in the LZ relation implies an evolution in the more fundamental mass-metallicity (MZ) relation. Development of more sophisticated models for stellar population synthesis (Bruzual & Charlot 2003) and gaseous nebula (Ferland 1996; Charlot & Longhetti 2001) allowed Tremonti et al. (2004, hereafter T04) to establish and quantify the local MZ relation for $\sim 53,000$ star-forming galaxies from the Sloan Digital Sky Survey. They found that metallicity increases linearly with mass for galaxies having masses between $10^{8.5} M_{\odot}$ and $10^{10.5} M_{\odot}$ and flattens out at higher masses. They attribute this depletion of metals in less massive galaxies to ubiquitous galactic winds that strip metals more effectively from galaxies with shallow potential wells, dispersing them into the IGM. Alternatively, it has been suggested that low mass systems have ongoing star formation and have yet to convert much of their gas into stars and therefore are not as metal-enriched as more massive galaxies

which have undergone rapid star formation. This "downsizing" scenario of galaxy evolution (Cowie et al. 1996) is supported by recent observational evidence (Juneau et al. 2005; Feulner et al. 2005; Franceschini et al. 2006; Pérez-González et al. 2008). Recently, a varying stellar mass distribution has also emerged as a possible explanation for the observed MZ relation (Köppen et al. 2007; Elmegreen 2009).

Observations of the MZ relation over cosmological timescales along with simulations may help to constrain various galaxy evolution scenarios. Moreover, cosmological hydrodynamic simulations (Brooks et al. 2007; Oppenheimer & Davé 2008) have predicted an evolution in the MZ relation and recent observations have provided strong evidence for an evolution. Using the Gemini Deep Deep Survey, Savaglio et al. (2005) first showed the MZ relation beyond the local universe out to intermediate redshifts of $0.4 < z < 1.0$. They observed a difference in metallicity of at most 0.1 dex at $z \sim 0.7$ and a slightly steeper slope as compared to the local sample of T04. Cowie & Barger (2008) found a difference of about 0.2 dex for a redshift range of $0.475 < z < 0.9$, but due to small sample size did not draw any strong conclusions on the evolution of the slope. More recently, Lamareille et al. (2009) find a flatter slope in the MZ relation out to $z \sim 0.9$ and an average difference in metallicity of ~ 0.2 dex. To date, the MZ relation has been extended beyond $z \sim 3$ (Erb et al. 2006; Maiolino et al. 2008; Shapley et al. 2005). All these studies have shown evidence of evolution but rigorous quantitative analysis has been hampered by disparate results and small sample sizes leaving the evolution in the MZ relation uncertain.

The effective yield has proven to be a useful diagnostic in understanding how galaxies deviate from "closed-box" evolution (Edmunds 1990). The effective yield can be calculated from observations of the metallicity and gas mass fraction. In the local universe, the effective yields have been observed to rise with increasing mass. This effect has been taken as evidence for the ubiquitous influence of galactic winds in shaping the MZ relation (Garnett 2002, T04). However, higher redshift studies have found the opposite trend (Erb et al. 2006; Mannucci et al. 2009). Given the uncertainties associated with the measurement of the effective yield the interpretation of this result remains unclear.

In this paper we present results of our study investigating the mass metallicity relation for galaxies in the redshift range of $0.75 < z < 0.82$. We infer metallicities from gas phase oxygen abundances using strong line diagnostics (Pagel et al. 1979; Kewley & Dopita 2002; Kewley & Ellison 2008). We make use of publicly available data from the Deep Extragalactic Evolutionary Probe 2 (DEEP2, Davis et al. 2003). We have metallicity measurements for 940 galaxies, an order of magnitude increase in the number of objects studied in this redshift range to date. We note that a large sample of galaxies with metallicity and stellar mass determinations in such small redshift range is ideal for investigating the MZ relation at higher redshifts. In §2 we present the publicly available data and our criteria for selection of galaxies in this study. In §3 we describe our method for determining masses and metallicities. In §4 we give results and discussion of the evolution of the MZ relation over cosmological timescales. In §5 we present results and discussion

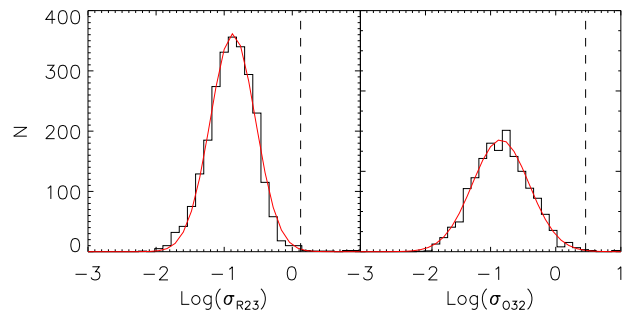


FIG. 1.— The distribution of errors in R_{23} (left) and O_{32} (right) for the DEEP2 survey sample. The red curve is a three parameter gaussian fit to the log of the error distribution. The dashed line is at the gaussian center + 3σ and is the upper limit for acceptable errors used in galaxy selection.

of the LZ relation and its evolution. In §6 we compare the MZ and LZ relations and attempt to resolve the discrepancy in the apparent metallicity evolution of the two relations. In §7 we calculate the gas mass and effective yield followed by a discussion in §8. We summarize our results in §9. Where necessary, we adopt the standard cosmology $(H_0, \Omega_m, \Omega_\Lambda) = (70 \text{ km s}^{-1} \text{ Mpc}^{-1}, 0.3, 0.7)$.

2. THE DEEP2 DATA AND SAMPLE SELECTION

The DEEP2 (Deep Extragalactic Evolutionary Probe 2) survey used the DEIMOS (Faber et al. 2003) multi-object spectrograph on the Keck telescope to measure spectra for galaxies in 4 fields covering 3.5 deg^2 down to a limiting magnitude of $R_{AB} = 24.1$. The survey contains spectra for $\sim 50,000$ galaxies, the majority of which are in the redshift range $0.7 < z < 1.4$. The relatively high-resolution ($R \geq 5000$) spectra cover the nominal spectral range 6500-9100Å. This spectral range corresponds to a redshift window of $0.75 < z < 0.82$ in which we observe the requisite lines for calculating the emission line ratios used in determining metallicity. BRI photometry was obtained by the DEEP team for these objects from imaging carried out using the CFH12K camera on the 3.6 m Canada France Hawaii Telescope (Coil et al. 2004). For a subsample of the data, K_s -band photometry was available in addition to the BRI photometry. These data were obtained using the Wide Field Infrared Camera on the 5m Hale telescope at Mt. Palomar (Bundy et al. 2006). The survey team determined confident redshifts for $\sim 30,000$ objects with 2,738 objects in our redshift range with lines in emission.

We measure the pseudo-flux¹ of emission lines for all galaxies with secure redshifts and within the redshift window allowing us to measure the emission lines used in the metallicity determination. In selecting galaxies from this sample for analysis, we require that the S/N for H_β be greater than 3. At high metallicities, the line strength of the [OII] and [OIII] line diminishes. In order to avoid biasing our metallicities and to keep it consistent with the selection of T04, we do not place a S/N cut on these lines. We identify all galaxies with $\text{log}(R_{23}) > 1$ as AGN and remove them from our sample (Kewley et al. in prep). We examine the distribution of errors in our pseudo-flux measurements for H_β , [OIII] $\lambda 5007$ and [OII] $\lambda \lambda 3726$,

¹ In the appendix we show that the pseudo-flux of a line is comparable to its equivalent width.

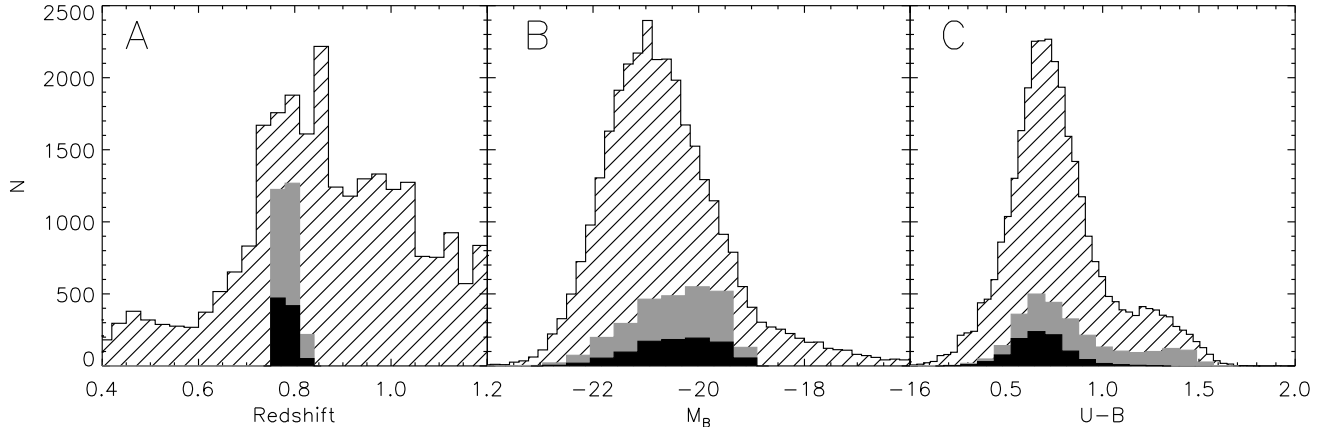


FIG. 2.— The redshift (Panel A), M_B (Panel B) and U-B color (Panel C) of galaxies in the survey sample. The hatched histogram in each plot represents the full DEEP2 sample, the grey represents the galaxies that are in our redshift range and have emission lines and the black represents the selected galaxies. In panels B and C the size of the bins in the emission line and selected sample histograms have been increased by a factor of 2.5 with respect to the full sample for ease of visualization on the given scale.

3728 and our calculated line ratios, R_{23} and O_{32} . We rely on the statistics of the error distribution to determine the appropriate data selection. For example, figure 1 shows that R_{23} and O_{32} measurements that are 3σ greater than the center of the normal distribution are removed from the sample. This selection procedure yields 971 galaxies from the original 2,738. A poorly detected continuum introduces significant error into our pseudo-flux determination. Any galaxy that does not have a mean continuum fit that is $1\sigma_c$ above 0 is excluded, where σ_c is error in the continuum (see appendix for more detail). This results in the removal of 31 galaxies, yielding a data sample of 940 objects.

Figure 2 shows the histogram of the redshift, the absolute extinction corrected B-band Magnitude and U-B color. We synthesize absolute magnitudes from a SED fit to our photometry (see § 3.1) convolved with filter functions given by Bessell (1990). The hatched histogram shows the whole survey, the grey histogram shows the 2,738 galaxies which were within our redshift range and for which we were able to measure emission lines and the black histogram shows the 940 galaxies that meet our selection criterion.

Panel B shows that the selected galaxies from the DEEP2 sample span a small range in absolute magnitudes, $-19.0 > M_B > -22.6$, compared with the full sample. The least luminous galaxies are only observed at the lowest redshifts in a magnitude limited sample and the most luminous galaxies are intrinsically rare and preferentially found at higher redshifts because of the larger volume. Because the redshift range for which we are able to measure metallicities is small compared to the full redshift range covered in the sample, the absolute magnitudes in our selected sample are not representative of the full DEEP2 sample (hatched histogram). Faber et al. (2007) show that luminosity functions derived from the DEEP2 sample have a $M_B^* = -21.15$ in our selected redshift range. We sample galaxies around the knee of the luminosity function (Schechter 1976) with $\sim 18\%$ of our galaxies brighter than M_B^* .

Panel C of figure 2 shows that the selected galaxies (black histogram) have a U-B color that is representa-

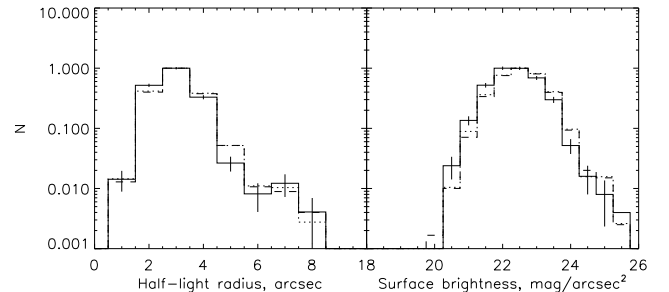


FIG. 3.— A normalized histogram of the half-light radius and R-band surface brightness distribution. The solid line is our selected sample, the dotted line is our emission line sample and the dashed line is the full sample. The solid vertical lines are the poisson errors for our selected sample.

tive of the the galaxies that fall in our redshift range and have measurable emission lines (grey histogram). The U-B color histogram shows that the galaxies we select from the larger sample preferentially pick out the bluer galaxies. Bluer galaxies will be those with the most star formation and therefore the strongest H_β emission. As can be seen by comparing the galaxies that fall in our redshift range and have emission lines (grey histogram) and those that we select (black histogram), the bluer galaxies are preferentially selected. Similar selection effects were found in the metallicity sample of the GOODS-N field (Kobulnicky & Kewley 2004) and the SDSS sample (T04).

In figure 3, we examine the half-light radius and R-band surface brightness distribution of our sample to examine selection biases that may result from the compactness or surface brightness of galaxies. The solid line in each of the plots is the normalized histogram for the 940 selected objects. The dotted curve is the emission line sample and the dashed curve is all the galaxies in our redshift range. The poisson errors for our selected sample are given by the vertical lines. From the left panel of figure 3 there does not appear to be any significant bias resulting from compactness of the source. The right panel in figure 3 does show that our selection is slightly biased towards higher surface brightness objects.

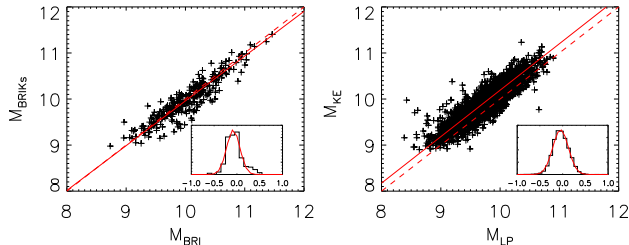


FIG. 4.— Comparison of stellar masses estimates. The left panel shows the mass estimates using BRI-band photometry (x-axis) as compared with $BRIS$ -band photometry (y-axis). The right panel compares mass estimates made using Le Phare and those used in T04. The dashed line in each plot is the one-to-one correspondence of the two methods. The solid line is a least-squares fit to the data. The left panel shows, to within the error, a one-to-one correspondence. In the right panel, the solid line is vertically offset from the one-to-one correspondence (dashed line) by 0.17 dex. The sub-panels in each of the plots shows a histogram of differences between the two estimates with 0.17 dex added to the Le Phare mass estimates in the right panel.

At a redshift of $z \sim 0.8$, observed R-band corresponds to rest-frame near ultraviolet. Similar to the color bias, we attribute this brightness selection effect to the fact that emission line galaxies are star-forming and will be rest-frame blue and UV bright. We note that this surface brightness analysis does not include galaxies that may be missing from the full DEEP2 survey due to low surface brightness (Impey & Bothun 1997).

3. DATA ANALYSIS

3.1. Mass determination

We estimate galaxy stellar masses by comparing photometry with stellar population synthesis models in order to determine the mass-to-light ratio (Bell et al. 2003; Fontana et al. 2004). We use the Le Phare² code developed by Arnouts, S. & Ilbert, O. to estimate the galactic stellar mass. The stellar templates of Bruzual & Charlot (2003) and an IMF described by Chabrier (2003) are used to synthesize magnitudes. We apply the extinction law of Calzetti et al. (2000) allowing $E(B-V)$ to range from 0 to 0.5 and an exponentially decreasing SFR ($SFR \propto e^{-t/\tau}$) with τ ranging from 0 to 13 Gyrs. A best fit of the synthesized magnitudes yields estimates for stellar mass and other physical parameters. Ilbert et al. (2009) provide a more detailed description of how stellar mass is estimated within the Le Phare code.

For 280 of our 940 galaxies we are able to determine masses using BRI and K_s -band data. In order to test for systematic variation in the mass determination for the remaining sample of galaxies with only BRI photometry, we compare the masses for our 280 galaxies determined with BRI and K_s -band data with masses determined with just the BRI-bands. The left panel of figure 4 shows the comparison. The dashed line is the one-to-one correspondence and the solid line is a linear fit to the data. The x-axis is the mass determination from BRI-band data and the y-axis is the mass determination from $BRIS$ -band data. The linear fit is given by

$$M_{BRIS} = (0.24 \pm 0.86) - (0.97 \pm 0.09)M_{BRI}, \quad (1)$$

² <http://www.cfht.hawaii.edu/~arnouts/LEPHARE/cfht-lephare/lephare.html>

where M_{BRI} and M_{BRIS} are the masses determined by using three and four bands respectively. The dispersion between the two methods is ~ 0.14 dex. The slope and intercept are within error of the one-to-one correspondence. We note that the lack of infrared photometry does not introduce any significant systematic variation in the mass determination. Surprisingly, the 3 optical (rest-frame UV) bands are sufficient to constraint the SED fit for determining masses of blue star-forming galaxies though with reduced uncertainty if infrared photometry is included.

In order to compare the MZ relation between different samples, care must be taken to ensure that both mass and metallicity are comparable. The masses in the local sample are derived using spectral indices (T04) and a Kroupa IMF (Kroupa 2001) whereas in the DEEP2 sample, we have used SED fitting and a Chabrier IMF. We test the comparability of the two methods by comparing mass estimates obtained using Le Phare and those used in the determination of the local MZ relation (T04). We use the Petrosian magnitudes given in the SDSS DR4 and correct for extinction using the prescription of Schlegel et al. (1998).

The right panel of figure 4 shows a comparison of mass estimates for the local sample made using Le Phare and those used in the determination of the local MZ relation (T04). The dashed line is the one-to-one correspondence and the solid line is a linear fit. The linear fit is given by

$$M_{LP} = (-0.01 \pm 0.10) + (1.02 \pm 0.01)M_{T04}, \quad (2)$$

where M_{LP} is the mass determined using Le Phare and M_{T04} is the mass used in the local MZ relation determined from spectral indices. The slope is near unity and we therefore determine that mass estimates differ by only a constant offset. This offset is attributed to the different IMF (Kroupa/Chabrier) and method (spectral/photometric) used in the two mass determinations. Adding 0.17 dex to the Le Phare masses brings them into one-to-one correspondence with the local MZ relation. The sub-panel in figure 4 shows the histogram of the differences between the two mass estimates once the 0.17 dex conversion is made. There is a 0.17 dex dispersion in the one-to-one correspondence.

It has been shown that the errors between photometric and dynamical mass are typically ~ 0.2 dex (Drory et al. 2004). Moreover, Conroy et al. (2009) have shown that additional uncertainties in estimates of physical parameters from stellar population synthesis modeling result from the choice of IMF, dust model and spectral libraries. However, the full impact of these effects on the absolute calibration of the physical parameters are still not well understood. Therefore, when investigating evolution of the MZ relation, we take care to calibrate the physical parameters between the samples. The absolute calibration remains uncertain.

3.2. Metallicity determination

We use the strong line diagnostics of Kobulnicky & Kewley (2004, hereafter KK04) as presented in Kewley & Ellison (2008, hereafter KE08) in order to obtain an estimate of galaxy gas-phase metallicities. The diagnostics are based on the Kewley & Dopita (2002) R23 theoretical calibrations. In both diagnostics the metallicity is

determined using the R_{23} and O_{32} ratios. We estimate the strength of an emission line by normalizing to the continuum and taking the area of the best-fit gaussian and refer to this as the pseudo-flux (for more details see Appendix). We calculate these ratios from our pseudo-fluxes such that

$$R_{23} = \frac{f_{p,OII} + f_{p,OIII}}{f_{p,H\beta}} \quad (3)$$

and

$$O_{32} = \frac{f_{p,OIII}}{f_{p,OII}}, \quad (4)$$

where

$$f_{p,OII} = f_p([OII]\lambda 3726) + f_p([OII]\lambda 3728), \quad (5)$$

$$f_{p,OIII} = 1.33 \times f_p([OIII]\lambda 5007), \quad (6)$$

and

$$f_{p,H\beta} = f_p(H\beta) \quad (7)$$

where $f_p(X)$ is the pseudo-flux measured for line X. For $f_{p,OIII}$ we have used the assumption that the ratio of the fluxes of $[OIII]\lambda 5007$ to $[OIII]\lambda 4958$ is 3 (Osterbrock 1989).

Metallicity is not a monotonically increasing function of R_{23} , but rather is doubly valued for a given ratio. A particular value of R_{23} corresponds to two different metallicities, one on the higher metallicity branch and one on the lower metallicity branch. The peak of the R_{23} ratio occurs at $12 + \log(O/H) \approx 8.4$. This degeneracy is due to the fact that on the lower branch R_{23} scales with metallicity because the intensity of the collisionally excited $[OII]$ and $[OIII]$ lines scales with the abundance. On the upper branch, nebular cooling, which is caused by collisional excitation followed by photon emission, effectively cools the nebula decreasing the electron temperature which leads to a decrease in the rate of collisional excitation of the $[OII]$ and $[OIII]$ lines. In order to break this degeneracy, generally other line ratios such as $[NII]/H\alpha$ are used. However, in our sample, these lines are not observed and the metallicity is assumed to lie on the upper branch. This assumption breaks down at lower masses and we revisit this issue in the following section.

4. MASS-METALLICITY RELATION

From our measured pseudo-flux and photometry, we can estimate both the masses and gas-phase oxygen abundances for the 940 galaxies in our sample. From the Spearman rank test, we conclude with over 99% confidence that we have a positive correlation between mass and metallicity. This confidence in our observed correlation justifies a fit to the data.

4.1. Fit to the MZ relation

The top panel of figure 5 shows mass and metallicity measured for our 940 galaxies. The bottom panel shows binned data with a boxcar smoothing. In determining the metallicity, we have assumed that all galaxies fall on the upper branch of the KK04 metallicity diagnostic. T04 have shown that in the local universe the MZ relation extends down to a stellar mass of $M_* = 10^{8.5} M_\odot$ with no break in the slope. We work under the assumption that the MZ relation at $z \sim 0.8$ extends to

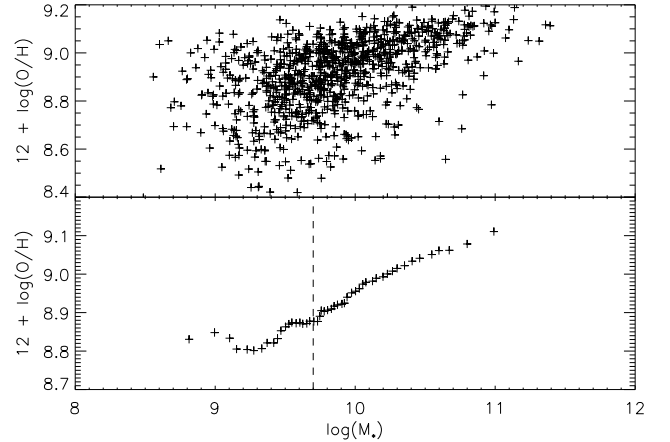


FIG. 5.— The mass and metallicity for the DEEP2 sample. The top panel shows the metallicity plotted against mass for the 940 galaxies in our sample. The bottom panel is a boxcar averaged smoothing of the data displayed in the top panel binned by mass. We attribute the break in the slope at $M \sim 10^{9.7} M_\odot$ to the misplacement of galaxies on the upper branch of the KK04 metallicity diagnostic. The vertical dashed line ($M = 10^{9.7} M_\odot$) in the lower panel is our lower limit cutoff mass used in determining the MZ relation for the DEEP2 sample.

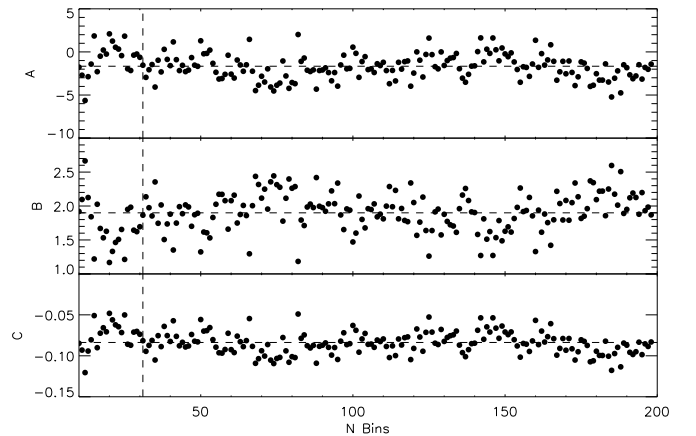


FIG. 6.— Variation of the quadratic fit parameters to the DEEP2 MZ relation defined in equation 8 as a function of number of bins. The horizontal dashed line is the average of the parameter over all bins. The vertical dashed line marks the adopted binsize used to display data.

at least $M_* \sim 10^9 M_\odot$ with no break in slope. Under this assumption, we interpret the break in the slope at $M_* = 10^{9.7} M_\odot$ observed in the bottom panel of figure 5 to be caused by the misplacement of lower branch galaxies on the upper branch (we return to this issue in § 4.2). We take a lower mass limit, indicated by vertical dashed line in the bottom panel of figure 5, of $M_* = 10^{9.7} M_\odot$ to fit our MZ relation. We note that 366 of our 940 galaxies fall below this limit, leaving us with 574 galaxies from which we determine the MZ relation.

Following T04, we parameterize the MZ relation with a quadratic function of the form

$$12 + \log(O/H) = A + Bx + Cx^2, \quad (8)$$

where $x = \log(M_*/M_\odot)$, the logarithm of the stellar mass in solar mass units. We determine the parameters and errors in our fit and test whether we are biased by

our binning method by fitting the MZ relation to binned data with different bin sizes. The data is binned by mass and the fitted points are the median of the mass and metallicity in each bin. The data is binned such that each bin contains the same number of data points and each bin shares 25% of the data with the adjacent bin. The bins vary in size such that the galaxies are sorted into 10 to 200 bins in mass. We emphasize that we only fit to data with $M_* \geq 10^{9.7} M_\odot$.

The three panels of figure 6 show the variation of the fitted parameters as defined in equation 8 as a function of increasing number of data bins. We perform a least-square polynomial fit using the *poly_fit.pro* routine in IDL with each bin weighted by its poisson error. For N values sorted by rank in each data bin, the 1σ upper and lower limit on the median is the $N/2 \pm \sqrt{N}$ data value respectively, where the $N/2$ data value is the median. In cases where we have a fractional bin value, the data is linearly interpolated. From this distribution we determine the parameters and errors by adopting the mean and standard deviation of the distribution as our parameter values and errors respectively. We determine the MZ relation to be

$$12 + \log(O/H) = -1.66 + 1.90x - 0.084x^2. \quad (9)$$

with the 1σ errors in each of the parameters in equation 9 given by $\sigma_A = 1.51$, $\sigma_B = 0.29$ and $\sigma_C = 0.014$. For display purposes, we show our data sorted into 31 bins (vertical dashed line, figure 6). The MZ relation fit by sorting data into 31 bins is consistent with our adopted values given in equation 9. The parameters calculated from a least-square fit to unbinned data differ by 1.1σ . We note that the least-square polynomial fit to the unbinned data is much more susceptible to influence of outliers (see top panel of figure 5) and fitting the median of data binned by mass is a more robust, outlier-resistant method.

4.2. R23 branch discrepancy

Under the assumption that the slope of the MZ relation extends below $M_* = 10^{9.7} M_\odot$ without a break, we can attribute the deviation from the MZ relation seen in the lower panel of figure 5 to galaxies misplaced on the upper branch. The observed MZ relation necessarily implies that the upper branch assumption will begin to break down at lower masses and the appearance of the knee in figure 5, we contend, corresponds to the mass where this effect becomes apparent. In order to test this hypothesis, we randomly select galaxies below $10^{9.7} M_\odot$ to be on the lower branch and rebin the data. We determine the optimum fraction of galaxies to place on the lower branch by averaging 1000 Monte Carlo realizations for each fraction and minimizing the RMS of the residuals of the binned data to the fitted quadratic MZ relation given in equation 9. We determine that the minimum mean RMS of the residuals is achieved by placing 16% of galaxies with $M_* < 10^{9.7} M_\odot$ (6% of full sample) on the lower branch with a lower branch probability increasing with increasing residual as $(Z(x) - z_i)^{0.65}$, where $Z(x)$ is the metallicity given by equation 9 and z_i is the measured metallicity of a galaxy at the same mass. This condition weights the probability of being on the lower branch by the amount a galaxy deviates from the derived MZ rela-

tion. Our derived lower branch frequency of 6% is less than the $>12\%$ and 17% values found by Caputi et al. (2009) and Maier et al. (2005) respectively. However, our selection is similar to T04 who find a lower branch frequency of 1.7%. The RMS of the residuals after 16% of galaxies are placed on the lower branch for the mass bins less than $10^{9.7} M_\odot$ is 0.025 dex.

Figure 7 displays the MZ relation with data displayed in 31 data bins. A total of 16% of the galaxies with $M_* < 10^{9.7} M_\odot$ (~ 60) have been placed on the lower branch. The solid curve is the quadratic fit determined from the mean of the parameters as they vary with the number of bins. The parameterization is given by equation 9. The dashed curve is the local MZ relation from SDSS as determined by T04 but with the metallicities converted to the KK04 metallicity diagnostic using the relations given in KE08 and comparable mass estimate (see §3.1). The T04 data have considerably smaller dispersion owing to the significantly larger sample size. The dotted curves show the 1σ uncertainties in the determined MZ relation displayed by the solid curve. The curve is well constrained between the range of the fitted data ($10^{9.7} M_\odot < M < 10^{10.9}$).

At the higher mass end the data are much more consistent with the local relation (~ 0.01 dex) than at the lower masses. This suggests that the highest mass galaxies have already achieved the level of enrichment observed in the local universe whereas the lower mass galaxies have yet to evolve to this level. Moreover, the flattening of the slope and the lack of evolution since $z \sim 0.8$ at the high mass end may suggest that there is a limit on the level of chemical enrichment obtainable by the most massive galaxies. We return to the discussion of the evolution in the MZ relation in §8.2.

5. LUMINOSITY-METALLICITY RELATION

Figure 8 shows the LZ relation derived from the DEEP2 sample and the local sample from SDSS. The filled circles are the median metallicities in 31 luminosity bins with a 25% overlap of data with neighboring bins, the same as the binning procedure used in determining the MZ relation. The solid curve is a linear fit (determined by the *linfit.pro* routine in idl) to the binned data and is parameterized by the equation

$$12 + \log(O/H) = (6.69 \pm 0.29) - (0.11 \pm 0.014)M_B. \quad (10)$$

The data points are weighted by their poisson errors. The dashed curve is the local LZ relation from SDSS calculated by the taking the median of metallicity in 30 magnitude bins. The local magnitudes have been determined using the same method as used in the DEEP2 sample for consistency. The local LZ relation is parameterized by the equation

$$12 + \log(O/H) = (7.10 \pm 0.035) - (0.095 \pm 0.002)M_B. \quad (11)$$

The slope of the two curves are consistent to within the errors. Because of the large sample size, the dispersion in the local relation is significantly smaller than in the $z \sim 0.8$ sample.

In figure 8, before we bin the data, we randomly place 16% of galaxies with masses less than $10^{9.7} M_\odot$ on the lower branch of the KK04 metallicity diagnostic. We test the stability of this procedure by performing 1000

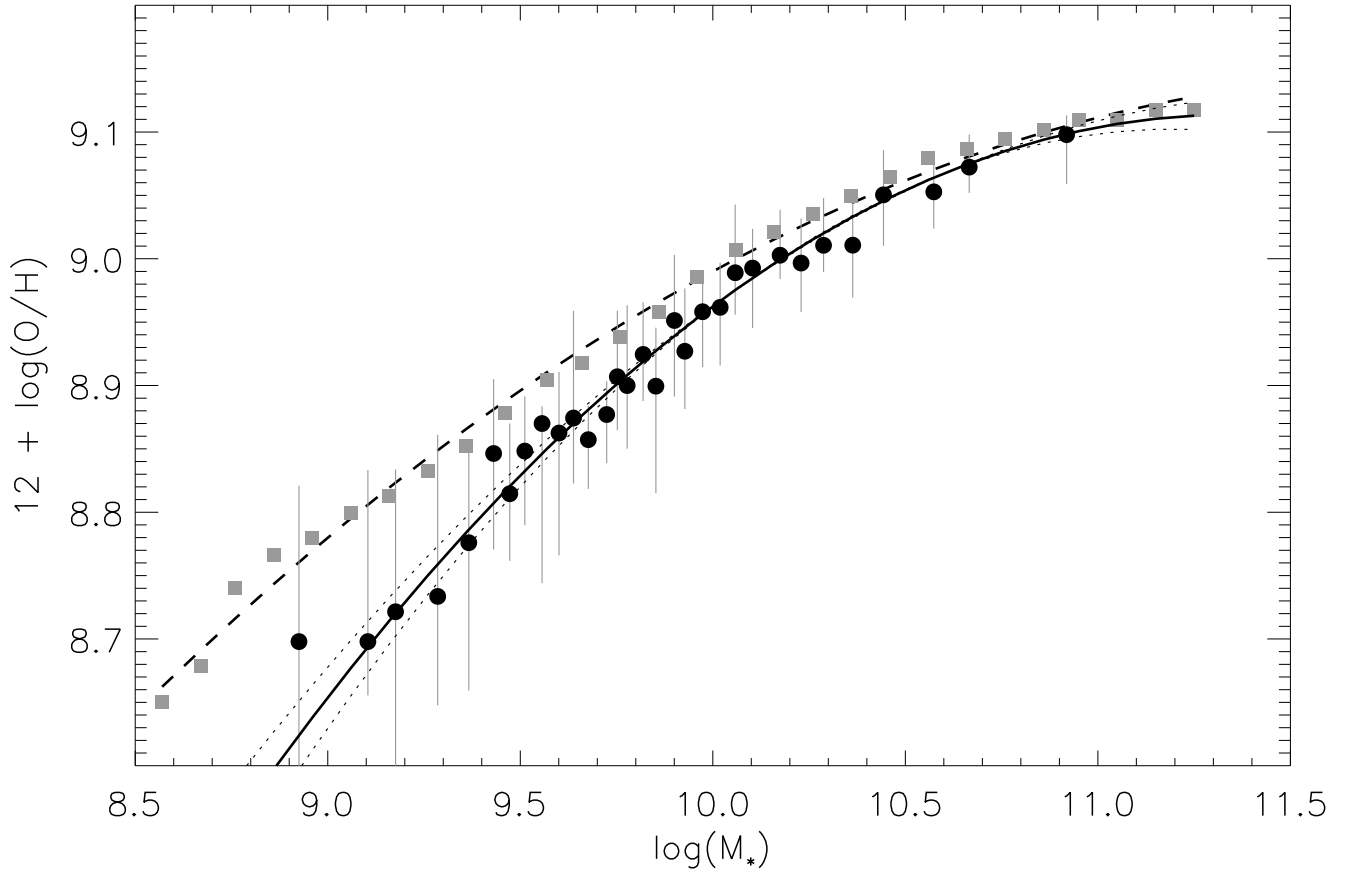


FIG. 7.— The MZ relation derived from the DEEP2 sample. The black data points are the median of the mass and metallicity sorted into 31 bins. The error bars are the 1σ poisson errors derived as explained in the text. A total of 16% of the galaxies below $M < 10^{9.7} M_{\odot}$ have been placed on the lower branch. The solid curve is a quadratic fit to the data as parameterized in equation 9. The dotted curves around the quadratic fit are the 1σ uncertainty curves derived from the 1σ uncertainties in the parameters. The dashed curve is the local MZ relation from T04.

realizations of the random selection and fitting a linear curve. We find that the intercept and slope of the linear fit for 1000 realizations have a standard deviation of 4.9×10^{-2} and 2.4×10^{-3} respectively. The parameters and errors given in equation 10 are the mean of the parameters and 1σ uncertainties of the linear fit for 1000 realizations. The mean standard deviation of the slope and intercept of the linear fit for the 1000 realizations is greater than the standard deviation of the fitted slope and intercept for the 1000 realizations showing that the error in our parameters is dominated by the measurement errors in the data and not errors introduced by the random placement of galaxies on the lower metallicity branch.

6. EVOLUTION OF LZ RELATION

In many previous studies, luminosity has been taken as a proxy for mass (Kobulnicky & Koo 2000; Pettini et al. 2001; Kobulnicky et al. 2003; Kobulnicky & Kewley 2004; Maier et al. 2004; Shapley et al. 2004, 2005). By comparing figures 7 and 8, we see that the offset in metallicity observed in the MZ relation is considerably smaller than the offset observed in the LZ relation. Except at the highest mass end where the DEEP2 sample suggest that the level of enrichment seen in the local sample has

already been reached at $z \sim 0.8$, the MZ relations differ by roughly constant offset of about ~ 0.05 dex, whereas the LZ relations are offset in metallicity by ~ 0.12 dex. Lamareille et al. (2009) interpret the differential evolution in the LZ and MZ as evolution of the mass-to-light ratio.

It has been shown that the luminosity functions of blue galaxies evolves with time (Willmer et al. 2006; Ilbert et al. 2006; Faber et al. 2007). We attribute the additional offset in the LZ relation to be caused by luminosity evolution in the sample of blue star-forming galaxies. In order to disentangle the evolution in metallicity from the evolution in luminosity, we begin by assuming that the metallicity evolution of star-forming galaxies can be characterized by the evolution of the MZ relation. We make a first order estimate of metallicity evolution to be 0.05 dex. In order to achieve rough agreement with the local LZ relation we have to add 0.8 mags to absolute B-band magnitudes of our sample. Figure 9 illustrates the procedure.

The evolution in the LZ relation observed can be attributed to evolution in both the metallicity and luminosity. To summarize, to first-order, we estimate that the metallicity of star-forming galaxies evolves by ~ 0.05 dex between the $z \sim 0.8$ and the local universe and the

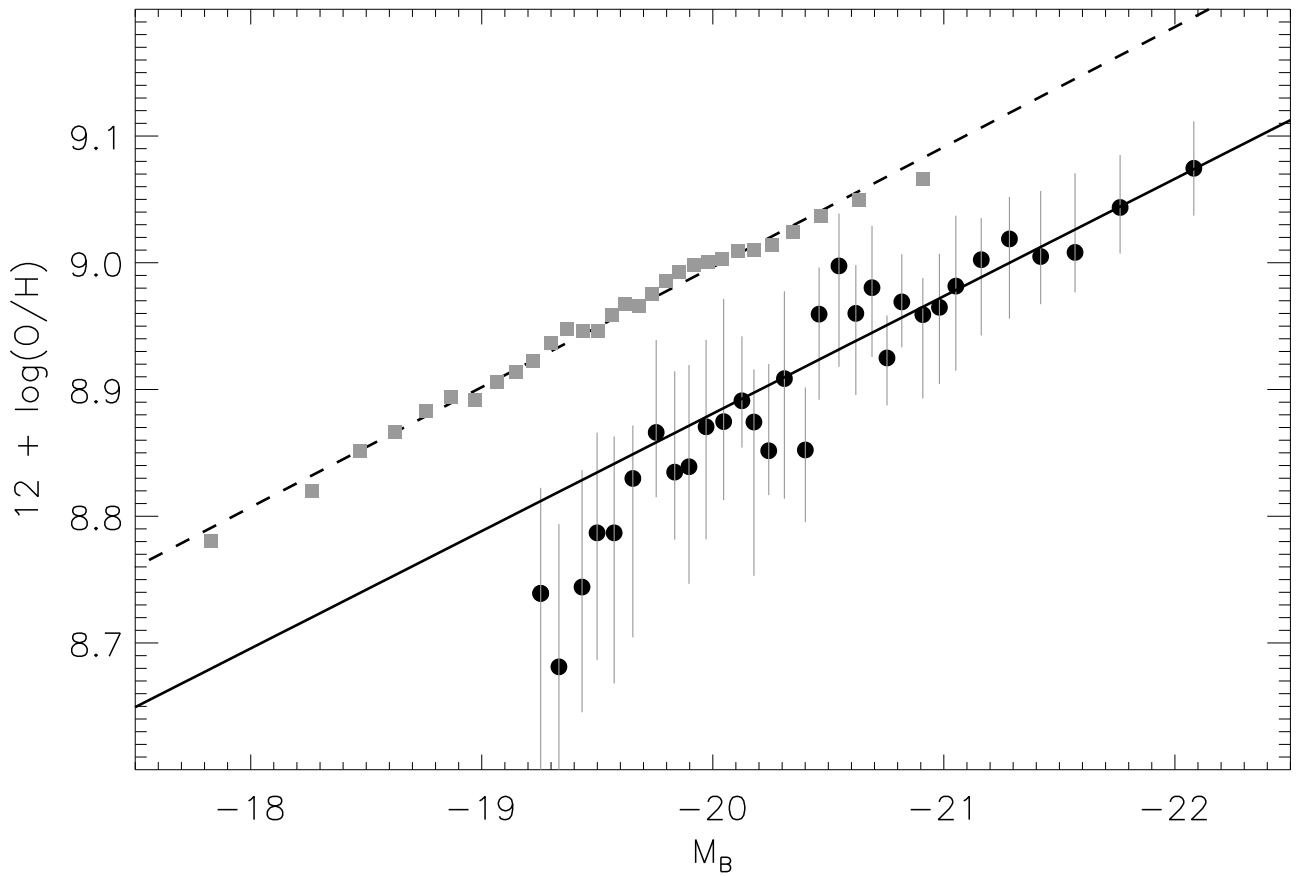


FIG. 8.— The LZ relation derived from the DEEP2 sample. The black data points are the median of the M_B and metallicity sorted into 31 bins. The error bars are the 1σ poisson errors. The solid line is a fit to the data as parameterized in equation 10. The squares are the median of the M_B and metallicity for the local LZ relation from SDSS sorted into 31 bins. The absolute B-band magnitudes have been determined to be consistent with the DEEP2 sample. The dashed line is the local LZ relation as parameterized by equation 11.

luminosity evolves by ~ 0.8 mags. We point out that this first-order treatment of the evolution in metallicity and luminosity mainly serves to highlight the difficulty in inferring chemical evolution from evolution of the LZ relation.

7. GAS MASS AND EFFECTIVE YIELD

7.1. Gas mass

We begin our investigation of the origins of the MZ relation by computing the gas mass fraction. The Schmidt star formation law relates the star formation rate to the gas mass (Schmidt 1959). Kennicutt (1998) determines this empirical relation for star-forming galaxies. We estimate the star formation rate from the $H\beta$ equivalent width and invert the Schmidt-Kennicutt relation in order to compute the gas mass. We derive the gas mass in terms of the star formation rate and the half-light radius. We note that this method is similar to the approach taken by T04, Erb et al. (2006) and Mannucci et al. (2009); the samples used for comparison in this study. The R-band half-light radius is measured by the DEEP2 team (Coil et al. 2004) and we determine the star formation rate using the relation presented in KK04, where

$$L_{H\beta}(\text{ergs s}^{-1}) = 5.49 \times 10^{31} \times 2.5^{-M_B} EW_{H\beta}. \quad (12)$$

Here the absolute B-band has been extinction corrected using the Calzetti extinction law (Calzetti et al. 2000). The star formation rate is given by

$$SFR(M_\odot \text{yr}^{-1}) = \frac{2.8 L_{H\beta}}{1.26 \times 10^{41}}. \quad (13)$$

We have taken the SFR given in Kennicutt (1998) and converted it to $H\beta$ luminosity by assuming that the luminosity of $H\beta$ is 2.8 times the luminosity of $H\alpha$. We make a 2\AA correction for Balmer absorption (Kobulnicky & Phillips 2003).

We assume an exponential disk model for the galaxy surface brightness,

$$I(r) = I_0 e^{-r/R_0}, \quad (14)$$

where I_0 is the central intensity and R_0 is the exponential scale length. We determine R_0 in terms of the observed half-light radius, r_h , where $R_0 = r_h / \ln(2)$. The observed R-band corresponds to rest-frame ultra-violet at $z \sim 0.8$. Muñoz-Mateos et al. (2007) show that small spiral galaxies have a large dispersion in the spatial gradient of the specific star formation rate (star formation rate per unit mass)-with no clear correlation to mass-with the gradients flattening out for more massive spiral galaxies. If the gradient of the specific star formation rate does not

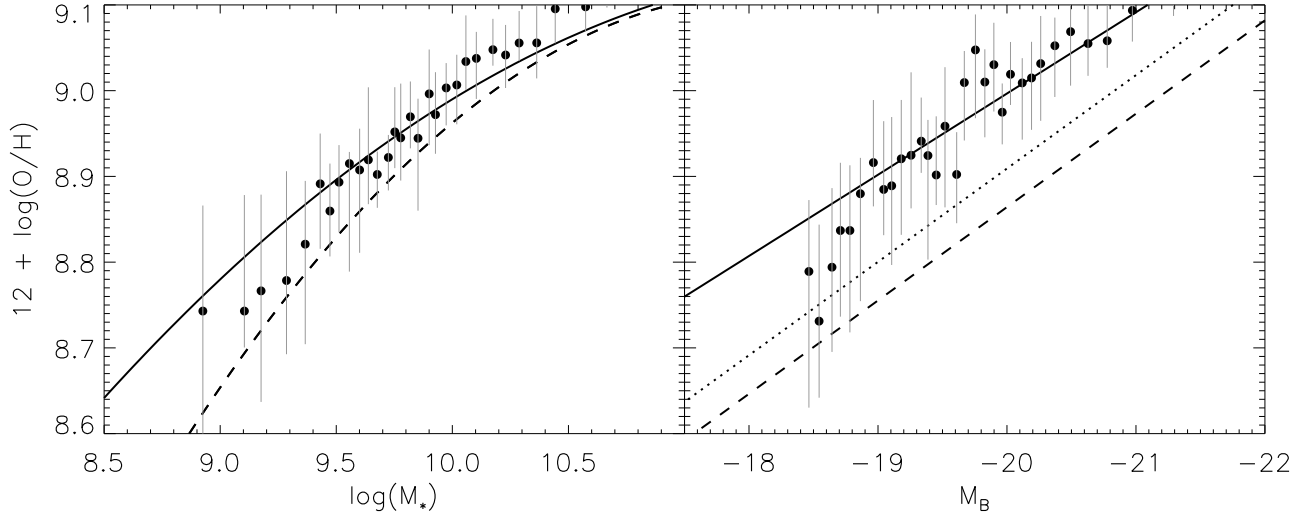


FIG. 9.— Inferred evolution in luminosity from the MZ and LZ relation. The left panel shows the MZ relation. The dashed curve is the DEEP2 MZ relation as shown in figure 7. The black data points are the the MZ relation with 0.05 dex added to bring them into rough agreement with the local MZ relation shown by the solid curve. The error bars are the 1σ poisson errors. The right panel shows the LZ relation. The lowest dashed curve is the DEEP2 LZ relation as shown in figure 8. The middle dotted curve is the LZ relation with 0.05 dex added to the metallicity. The solid line is the local LZ relation and the black points are the DEEP2 data with 0.05 dex added to metallicity and 0.8 mags added to M_B . The error bars are the 1σ poisson errors.

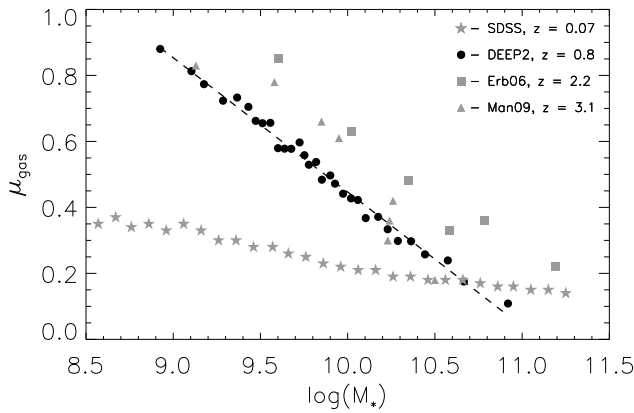


FIG. 10.— The gas fraction as a function of stellar mass. The gas fractions are inferred by inverting the Schmidt-Kennicutt star formation law. The black data points are the median of the gas fraction sorted into 31 mass bins. The dashed curve is a linear fit to the data. The grey stars, squares and triangles are the data from T04, Erb et al. (2006) and Mannucci et al. (2009) respectively.

change systematically and the Schmidt-Kennicutt relation holds, we are justified in assuming that the gas density scales with the UV intensity. Because we are attempting to measure the gas fraction for galaxies in a statistical sense, we assume the star formation surface density, Σ_{SFR} , scales with the intensity with the same scale length, R_0 . The star formation surface density is then given by

$$\Sigma_{SFR}(r) = S_0 e^{-r/R_0}, \quad (15)$$

where S_0 is determined by integrating the star formation surface density,

$$\int_0^{r_h} S_0 e^{-r/R_0} 2\pi r dr = \frac{1}{2} SFR, \quad (16)$$

where SFR is given by equation 13.

We invert the Schmidt-Kennicutt relation to obtain surface density of gas, Σ_{gas} in terms of the surface density of star formation. This gives

$$\Sigma_{gas}(r) = \left(\frac{1.8 \times 10^{12} \Sigma_{SFR}(r)}{M_\odot \text{ yr}^{-1} \text{ kpc}^{-2}} \right)^{0.71} M_\odot \text{ kpc}^{-2} \quad (17)$$

$$= 5.1 \times 10^8 \left(\frac{S_0 e^{-r/R_0}}{M_\odot \text{ yr}^{-1} \text{ kpc}^{-2}} \right)^{0.71} M_\odot \text{ kpc}^{-2}, \quad (18)$$

where the constant of proportionality given by Kennicutt (1998) of 2.5×10^{-4} becomes 5.5×10^{-13} when gas surface density is given in $M_\odot \text{ yr}^{-1}$ and a factor of 1.8 for the change from a Salpeter to Chabrier IMF (Erb 2008). We integrate the gas surface density to get the total gas mass, given by

$$\frac{1}{2} M_{gas} = \int_0^{r_h} \Sigma_{gas}(r) 2\pi r dr M_\odot \quad (19)$$

$$M_{gas} = 8.5 \times 10^8 \left(\frac{SFR}{M_\odot \text{ yr}^{-1}} \right)^{0.71} \left(\frac{r_h}{\text{kpc}} \right)^{0.58} M_\odot. \quad (20)$$

We calculate a gas fraction, μ_{gas} , such that

$$\mu_{gas} = \frac{M_{gas}}{M_{gas} + M_*}. \quad (21)$$

Figure 10 shows the gas fraction as function of the stellar mass. All mass estimates have been converted to be consistent amongst the samples. The dashed curve is a linear fit (determined by the *linfit.pro* routine in *idl*) to the data with

$$\mu_{gas} = (4.52 \pm 0.08) - (0.41 \pm 0.01)x, \quad (22)$$

where x is the logarithm of the stellar mass in solar mass units as previously defined. The gas fraction is lowest for the local sample. The slope of the gas fraction as a

function of stellar mass is consistent between the $z \sim 3.1, 2.2$ and 0.8 samples with small offsets between the three. The slope of the gas fraction as a function stellar mass is considerably shallower for the local sample with a large change since $z \sim 0.8$.

The correlation between the gas mass fraction is remarkably tight given the large uncertainties associated with the Schmidt-Kennicutt law. We note that the absolute B-band magnitude is used in inferring the SFR given by equation 13. We attribute much of the small dispersion in the correlation of the gas fraction with the stellar mass to the correlation of the stellar mass and the absolute B-band magnitude, though at $z = 1.5$, Daddi et al. (2009) find a tight correlation between gas mass, inferred from CO luminosity, to stellar mass, using the UV. Figure 10 shows the gas mass decreasing linearly with increasing mass, consistent with observations (McGaugh & de Blok 1997; Kannappan 2004) and model predictions (Brooks et al. 2007; Mouchine et al. 2008) and the expectation that less massive galaxies have yet to convert much of their gas into stars.

7.2. The effective yield

From a closed box model, as gas is converted into stars and then dispersed back into the ISM through various mass loss processes, one would expect the overall gas phase metallicity to increase with time. Edmunds (1990) defines the closed box model by

$$d(M_{gas}Z) = p'ds - \alpha Zds, \quad (23)$$

where M_{gas} is taken to be the gas mass, Z the mass fraction of heavy elements and $p'ds$ is the mass of heavy elements produced and instantaneously recycled into ISM. A fraction, α , of the gas is not recycled into the ISM but forms into stars and remains locked up in low mass stars or stellar remnants. For the closed box where there is no mass loss or gain, the stellar and gas mass are related by

$$dM_{gas} = -\alpha ds \quad (24)$$

With this assumption and the assumption that the system begins with no stars or heavy elements, the solution to equation 23 is

$$Z = y_0 \ln(\mu_{gas}^{-1}) \quad (25)$$

where y_0 , the true stellar yield, is the ratio of the mass in heavy elements to the stellar mass, p'/α . It can be seen from equation 25 that in a closed system the metallicity increases as gas fraction decreases (i.e. as gas is converted into stars).

However, galaxies are known not to evolve as closed systems. A useful diagnostic for understanding the contributions of feedback and inflow is the "effective yield" (Edmunds 1990; Dalcanton 2007). Inverting equation 25 gives

$$y_{eff} = \frac{Z}{\ln(\mu_{gas}^{-1})}, \quad (26)$$

where the effective yield can be calculated from our measurements of metallicity and gas mass fraction. Following KK04, we take the metal mass fraction to be

$$Z = 29 \times 10^{(12 + \log(O/H) - 12)}. \quad (27)$$

When the assumptions of the closed box model hold the effective yield is equal to the true yield, y_0 .

Figure 11 shows the effective yield for our sample. The metallicities in each of the samples have been converted to be consistent with the KK04 diagnostic (Kewley & Ellison 2008) and the mass estimates are consistent. The black filled circles are the median effective yields in 31 mass bins. The grey stars are the effective yields from T04, the grey squares are the effective yields from Erb et al. (2006) at a redshift of $z \sim 2.2$ and the grey triangles are the effective yields from Mannucci et al. (2009) at a redshift of $z \sim 3.1$. The dashed curve is a quadratic fit to our data and is given by

$$\log(y_{eff}) = 9.92 - 1.95x + 0.080x^2, \quad (28)$$

where the 1σ errors of the three coefficients are 2.62, 0.53 and 0.027 respectively with x being previously defined.

The behavior of decreasing effective yield with increasing stellar mass is consistent in the three higher redshift samples and is close to flat for the local sample³. There is remarkable agreement between the Erb et al. (2006) sample and ours. The Mannucci et al. (2009) sample is lower because of its considerably lower metallicity but only slightly higher gas fraction as compared to $z \sim 2.2$ and 0.8 . The reasonable agreement of the effective yield at the high mass end between the T04, DEEP2 and Erb et al. (2006) suggest that the relative calibration may be consistent. However, we note that there is considerable uncertainty in the absolute calibration of the effective yield due to uncertainties in the absolute calibration of metallicity and estimates of gas fraction.

8. DISCUSSION

We begin by noting that the MZ relation does not trace the evolution of particular galaxies over time. In fact, most of the population of star-forming galaxies comprising the DEEP2 sample at $z \sim 0.8$ have likely evolved to the red sequence. In this context, evolution of the MZ relation results from the evolution of the population of star-forming galaxies and their environments.

8.1. Assumptions

We list and address some key assumptions made in this paper:

1. All galaxies with $M_* \geq 10^{9.7} M_\odot$ are on the upper branch of the R_{23} diagnostic and the slope of the MZ relation is continuous down to at least $M_* \sim 10^9 M_\odot$. T04 show that for mass bins with $M_* = 10^{9.7} - 10^{11} M_\odot$ the 1σ dispersion in the metallicity is 0.15 - 0.07 dex. At $M_* = 10^{9.7} M_\odot$ we have a $12 + \log(O/H) \sim 8.9$, which is $> 3\sigma$ from the lower branch metallicity of 8.4. Additionally, T04 have observed a continuous slope down to $M_* \sim 10^{8.5} M_\odot$ so these assumptions seem reasonable (see § 4.2).

2. Metals are instantaneously recycled and α and p' in equation 23 are not explicitly dependent on time. This approximation was first introduced by Schmidt (1963). The approximation is valid when metals produced in

³ The effective yield for the local sample in figure 11 is different from figure 8 of T04 because of the conversion of the metallicity to the KK04 diagnostic and the use of the stellar mass as opposed to baryonic mass.

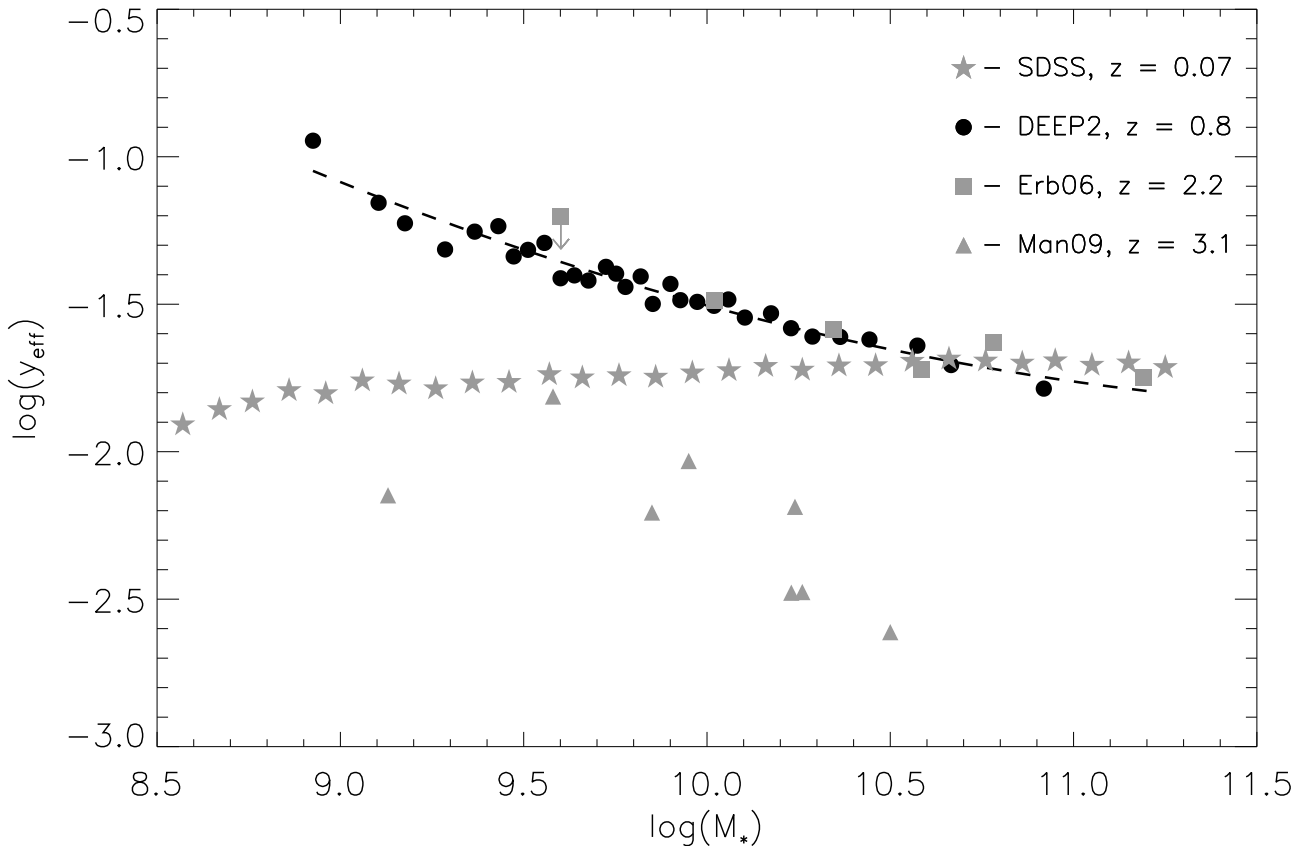


FIG. 11.— The effective yield as a function of stellar mass. The black filled circles are the median of the gas fraction sorted into 31 mass bins for our data. The grey stars, squares and triangles are the data from T04, Erb et al. (2006) and Mannucci et al. (2009) respectively. All metallicities are calculated to be consistent with the KK04 diagnostic and the gas mass is inferred in all samples using the Schmidt-Kennicutt star formation law (Kennicutt 1998).

massive stars, such as oxygen, are considered and if the SFR is not subject to extreme variations on short timescale (Pagel 1997). This assumption is appropriate for the DEEP2 sample.

3. The Schmidt-Kennicutt star formation relation is valid. Bouché et al. (2007) have shown tight correlation between gas surface density and star formation rate surface density for high surface density galaxies at $z \sim 2$, though with a slightly steeper slope. Tacconi et al. (2010) have directly observed star forming galaxies at $z \sim 2$ to be gas rich and, to within the uncertainties, find the Schmidt-Kennicutt relation to be independent of redshift. We adopt the slope determined by Kennicutt (1998) for our $z \sim 0.8$ sample (see § 7.1). This is consistent with T04, Erb et al. (2006) and Mannucci et al. (2009).

4. We have attempted to remove AGN using empirical limits on the R_{23} ratio. This removes most of the galaxies whose emission is dominated by AGN, but composite galaxies in our sample may not exceed the empirical R_{23} limit. AGN contamination in composite galaxy spectra increases the R_{23} ratio due to the high ionized oxygen to $H\beta$ emission ratio. On the upper metallicity branch of the R_{23} diagnostic, the metallicity is a monotonically decreasing function of R_{23} . Therefore, AGN contamina-

tion will lower the metallicity estimate. The continuum UV emission of a AGN can be characterized by a power-law. The observed BRI-band photometry corresponds to rest-frame UV and blue emission. We have inferred stellar mass from the comparison of photometry with stellar population synthesis models (as described in § 3.1) which assumes a pure star forming population. This results in an overestimate of mass when AGN contamination is present. AGN contamination therefore results in an overestimate of the stellar mass and an underestimate of the metallicity. This compounds to make AGN contaminated galaxies fall below the emission line galaxy MZ relation by moving galaxies down and to the right in a plot of metallicity vs. mass (see figures 5 and 7). However, due to their relatively small numbers and the small dispersion in the MZ relation, AGN contamination is most likely negligible in the determination of the MZ and LZ relations (Lamareille et al. 2009).

5. Since its introduction by Salpeter (1955), the initial stellar mass function (IMF) - describing the mass distribution of stars - has largely been taken to be universal and invariant. Despite the large body of literature attempting to explain this, the invariance of the IMF still lacks a solid theoretical foundation (see Bonnell et al. 2007, and references therein). Moreover, observational evidence is mounting for a varying IMF (e.g. Elmegreen

2009). Indirect evidences for variations in the local IMF have been provided by the comparison of $H\alpha$ emission to the far-ultraviolet flux (Meurer et al. 2009) and the $H\alpha$ flux to broadband color index (Hoversten & Glazebrook 2008). Comparisons of the rate of luminosity evolution to the rate of color evolution provides indirect observational evidence for a possible redshift evolution in the IMF (van Dokkum 2008).

In the context of galactic chemical evolution, a varying galaxial stellar mass distribution would have significant implications. Weidner & Kroupa (2005) show that the integrated galaxial mass function (IGIMF) - the mass distribution of stars within a galaxy - is the distribution of interest for understanding the chemical enrichment history of galaxies. Lada & Lada (2003) have shown that the vast majority of stars are formed in embedded clusters. The IGIMF can then be approximated by the integral of the IMF over the embedded cluster mass function (ECMF). Within this framework, even a universal IMF could lead to invariance in the stellar mass distribution due to variations in the ECMF. The possible variation of the mass distribution of stars within galaxies is a critical issue for understanding the chemical evolution of galaxies and its full implications remain to be worked out. It is beyond the scope of this study to attempt to address these issues though our future work modeling the observations in this and similar studies will explore these ideas.

6. MZ and LZ relation studies assume that the absence of low surface brightness galaxies (LSBGs) do not significantly bias the determination of the MZ and LZ relations. Impey & Bothun (1997) point out that LSBGs will be absent in magnitude limited surveys. LSBGs tend to have a bright core surrounded by diffuse disk. The angular extent of the bright core at $z \sim 0.8$ is significantly smaller than in the local universe and may be a small fraction of a pixel. Therefore, in a magnitude limited sample, the surface brightness selection bias is likely a function of redshift. From SDSS, the metallicity and stellar mass of LSBGs is shown to decrease with smaller surface brightness (Zhong et al. 2008; Liang et al. 2009). These results show that at $M_* \gtrsim 10^{10.2} M_\odot$ there is no strong correlation between surface brightness and stellar mass, suggesting that we are unlikely to be affected by a strong LSBG selection bias at the high stellar mass end. However, at lower stellar masses, owing to possible redshift dependence of surface brightness effects, the samples may not be comparable. This effect cannot be quantified at this time with the DEEP2 dataset and we await surface brightness limited surveys to resolve this issue.

8.2. Origin of the MZ relation

Several ideas have emerged in the literature on the origin of the MZ relation. The inability for less massive galaxies to retain their metals due to their shallow potential wells has been cited by several authors as a possible origin (Larson 1974; Dekel & Silk 1986; Garnett 2002; Tremonti et al. 2004; Kobayashi et al. 2007; Finlator & Davé 2008). Dalcanton et al. (2004) argue that in low mass galaxies, the star formation timescale may be greater than the gas accretion timescale and that the infall of pristine gas could suppress the metallicities of

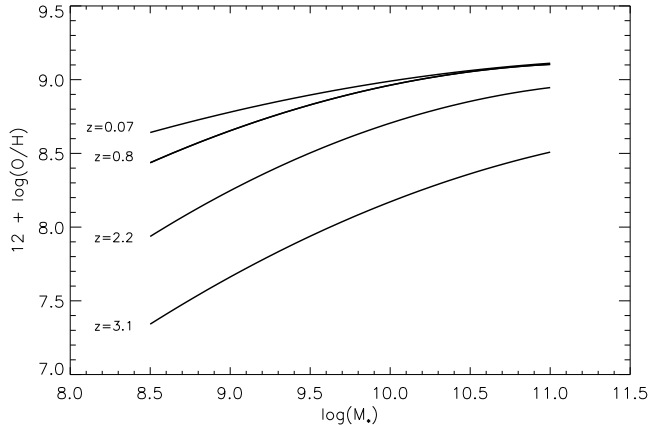


FIG. 12.— The MZ relation at a redshift of 0.08, 0.8, 2.2 and 3.1 from T04, our own study, Erb et al. (2006) and Mannucci et al. (2009) respectively. The mass and metallicities have been converted to make the measurements consistent.

these systems causing the observed MZ relation. Another possibility is the lower efficiency of low mass galaxies in producing stars. In this interpretation, low mass galaxies are considered to be less evolved and therefore have lower metallicities in relation to higher mass, more evolved, galaxies (Brooks et al. 2007; de Rossi et al. 2007; Mouchine et al. 2008; Calura et al. 2009). Finally, Köppen et al. (2007) have shown that models with non-universal IMF where less massive galaxies produce less massive stars can reproduce the observed MZ relation.

On the basis of an increasing effective yield with larger baryonic mass, T04 argue that galactic winds may be the cause of the MZ relation. Looking at figure 11 and comparing to figure 8 of T04 we find that by converting metallicities to the KK04 diagnostic, we significantly reduce the slope of the effective yield as function of mass. To date it is still unclear which of the many metallicity diagnostics most accurately reproduces the actual metallicity in an absolute sense (KE08) and therefore the true behavior of the effective yield as a function of mass is uncertain. By examining the relation between effective yield and rotational velocity, Garnett (2002) came to a similar conclusion as T04. However, analyzing the same data, Dalcanton (2007) showed the suppressed effective yield could be caused by inflow of gas. Observations of a MZ relation with a similar slope at higher redshifts (see figure 12) but with an opposite trend in effective yield (see figure 11) taken together with simulations (de Rossi et al. 2007; Brooks et al. 2007; Mouchine et al. 2008) suggests that neither galactic winds nor the infall of un-enriched gas play a significant role in shaping the MZ relation, though they probably play a dominant role in shaping the mass-effective yield relation through regulation of the gas fraction.

The role of gas flows may be inconsequential in shaping the MZ relation. If so, a non-universal galaxial stellar mass distribution or a rising efficiency of star formation with larger stellar mass may emerge as the cause of the MZ relation. However, a variation in the mass distribution of stars as a function of both galactic stellar mass and redshift in the context of galactic chemical evolution requires a more solid theoretical and observational foundation. A changing star formation efficiency is

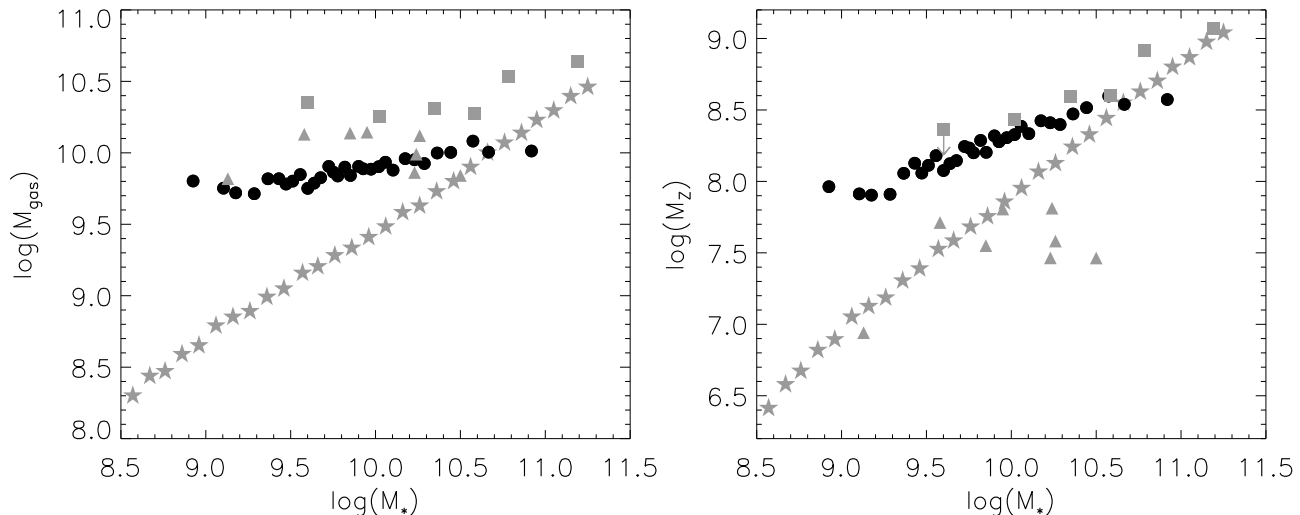


FIG. 13.— The mass of gas (left panel) and metals (right panel) as a function of stellar mass. The gas mass is inferred from the Schmidt-Kennicutt star formation law and the mass of metals is inferred thereafter from the metallicity. The grey stars, squares and triangles are the data from T04, Erb et al. (2006) and Mannucci et al. (2009) respectively.

supported by hydrodynamical simulations (Tissera et al. 2005; de Rossi et al. 2007), cosmological N-body simulations (Brooks et al. 2007; Mouchine et al. 2008; Tassis et al. 2008) and chemical evolution models (Lequeux et al. 1979; Matteucci 1994; Calura et al. 2009) but is lacking solid observational support.

8.3. Chemical enrichment evolution

Figure 12 is similar to figure 5 of Mannucci et al. (2009) and shows the MZ relation at a redshift of 0.07, 0.8, 2.2 and 3.1 from T04, our own study, Erb et al. (2006) and Mannucci et al. (2009) respectively. All observations have been converted to have consistent mass and metallicity estimates. Figure 12 shows an offset of ~ 0.6 dex between the redshifts of 3.1 and 2.2, ~ 0.4 dex between redshifts of 2.2 and 0.8 and ~ 0.05 dex between redshift of 0.8 and 0.07.

For the purpose of argument, we assume that the change in the mass-effective yield relation over cosmological time is real and tentatively explore possible reasons for the change in slope. The negative slope in the mass-effective yield relation is attributed to galactic scale outflows by Erb et al. (2006) and unenriched gas inflows by Mannucci et al. (2009) for their samples respectively. In order to make the observed mass-effective yield relation at $z \sim 0.8$ consistent with the local mass-effective yield relation, we have to reduce the effective yield at the low mass end of our sample. At the low mass end, we have a high gas fraction and as Dalcanton (2007) shows

$$y_{eff} \approx \frac{M_Z}{M_*}, \quad (29)$$

where M_Z is the mass of metals. The metallicity is given by

$$Z = \frac{M_Z}{M_{gas}}. \quad (30)$$

In gas-rich systems, the effective yield is essentially independent of the gas mass. From equation 29 we see

that for gas rich (low stellar mass) systems the effective yield can only become smaller if the stellar mass gets larger and/or the mass of metals gets smaller. In order for the effective yield to become smaller at a constant stellar mass at the low mass end between $z = 0.8 - 0.07$, the total mass of metals, M_Z , must also become smaller. However, from the MZ relation we have learned that the gas-phase oxygen abundance at the low mass end rises due to chemical enrichment between $z = 0.8 - 0.07$ (see figure 7). The only way the observation of a decreasing metal mass can be reconciled with an increasing gas-phase oxygen abundance is if the mass of gas is depleted by a larger fraction than the mass of metals. This effect could be possible in light of the observations of a decreasing star formation rate (Arnouts et al. 2005; Le Floch et al. 2005; Hopkins & Beacom 2006; Reddy et al. 2008) and, from theoretical considerations, a decreasing gas accretion rate with time (Neistein et al. 2006; Genel et al. 2008). To account for the ~ 0.05 dex mean difference in metallicity, the relative gas mass would have to be depleted by $\sim 12\%$ more than the relative mass of the metals over this redshift range. Unlike the slope of the MZ relation (see § 8.2), this depletion suggests that the slope of our observed mass-effective yield relation at $z \sim 0.8$ is likely dominated by gas outflows.

Perhaps a more intuitive way to understand the effective yield is to consider the mass of gas and mass of metals directly. Here, the gas mass is given by equation 20 and the mass of metals is taken from equation 30. Figure 13 shows the mass of the gas and metals as a function of stellar mass. We have calculated the mass of metals from the oxygen abundances assuming that the total metal fraction is well represented by the oxygen abundance. The absolute value of M_Z may be uncertain but the relative differences are likely to be real. In the non-local samples, the gas mass is nearly constant with respect to stellar mass. At a fixed stellar mass, there is a modest fractional rise in the gas mass in the epoch between $z = 3.1 - 2.2$ as can be seen in the left panel of figure 13. Conversely there is a rather large fractional rise

in the mass of metals during this same period. The observed evolution in the MZ relation in the epoch between $z = 3.1 - 2.2$ can be explained by a rise in the gas mass, coupled with a larger rise in the mass of metals implying star formation and gas accretion. These conclusions are consistent with the findings of Mannucci et al. (2009).

Somewhat surprisingly, in the epoch between $z = 2.2 - 0.8$ and $z = 0.8 - 0.07$, at a fixed stellar mass, both the mass of gas and mass of metals *decreases*. If this is true, then the observed chemical enrichment (see figure 12) is not the result of a rise in the absolute metal content of galaxies, but rather, is a consequence of a fractional rise in the metals with respect to the gas, though both are depleted. Gas outflows coupled with star formation may be responsible for such an effect, a finding consistent with the conclusions of Erb et al. (2006). The differential evolution in the MZ relation, observed as a change in the slope, suggest that galaxies at lower masses are becoming relatively more enriched as compared to higher mass galaxies, consistent with the downsizing hypothesis (Cowie et al. 1996). Our future work will attempt to confront these observations with models.

9. SUMMARY

We have conducted a study of the mass-metallicity and luminosity-metallicity relation at $z \sim 0.8$ using the 940 galaxies from the DEEP2 survey. The large sample in a small redshift range is ideal for this type of analysis. We have obtained masses by inferring a SED from our photometry and fitting it with stellar population synthesis models. We have estimated gas mass fractions by inverting the Schmidt-Kennicutt star formation law and have obtained estimates of the effective yield. We summarize our conclusions as follows:

1. We find a clear correlation between mass and metallicity at $z \sim 0.8$, consistent with previous work (Savaglio et al. 2005; Cowie & Barger 2008; Lamareille et al. 2009). The level of chemical enrichment achieved by galaxies decreases with decreasing mass. Galaxies at $M_* > 10^{10.5}$ have achieved the level of enrichment observed in the local universe and the flattening of the relationship suggests there may be an upper limit to galactic metallicity. Galaxies with $M_* < 10^{10.5} M_\odot$ have yet to achieve the level of enrichment observed in the local universe and differ by a mean metallicity of ~ 0.05 dex. The slope of the MZ relation is steeper at $M_* < 10^{10.5}$ than that observed in the local universe.

2. There is a clear correlation between luminosity and metallicity at $z \sim 0.8$. The level of enrichment achieved by galaxies decreases with decreasing luminosity. The metallicity at a given luminosity at $z \sim 0.8$ is ~ 0.12 dex smaller than the local relation. We attribute the additional difference of ~ 0.7 dex when compared to the MZ relation to luminosity evolution in the population of star-forming galaxies. Lamareille et al. (2009) have pointed out that this suggests an evolution in the mass-to-light ratio. We estimate the B-band luminosity evolution to

be ~ 0.8 mags. The slope of the LZ relation at $z \sim 0.8$ is consistent to within the errors to what is observed in the local universe.

3. The effective yield measures the amount that galaxy evolution deviates from a closed box type of evolution. Unlike the local universe where the effective yield is found to rise with increasing mass, we find the effective yield decreases at larger stellar masses at $z \sim 0.8$. This finding is qualitatively consistent with the studies of Erb et al. (2006) and Mannucci et al. (2009) at $z \sim 2.2$ and 3.1 respectively. The changing qualitative behavior of the effective yield with stellar mass, taken together with the modest change observed in the MZ relation between $z = 0.8 - 0.07$ downplays the role of gas flow in shaping the MZ relation. If gas flows are not the dominant physical mechanism shaping the MZ relation, then a rising star formation efficiency with rising stellar mass or a non-universal IGIMF emerge as the most likely causes of the MZ relation.

4. The observed chemical enrichment in the epoch between $z = 2.2 - 0.8$ and $z = 0.8 - 0.07$ appears to be the result of a relative rise in the metal content with respect to the gas content, but an absolute depletion of both.

In light of the observations of the MZ relation and the effective yields at higher redshifts, one would expect that at some intermediate time between $z \sim 0.8$ and the present, there was a change in the qualitative behavior of the gas flows governed by infall and galactic winds. It will be interesting to see if studies in this intermediate redshift range bear out this expectation. Our study also suggest a decreasing metal and gas mass for galaxies at a fixed stellar mass as they evolve to what is observed in the local universe. However, these observations are quite uncertain and the results are heuristic at best. Higher quality observations of the metallicity and gas fractions will help in quantifying and testing the results presented in this and similar studies.

We thank the DEEP2 team for making their data publicly available. The analysis pipeline used to reduce the DEIMOS data was developed at UC Berkeley with support from NSF grant AST-0071048. We also thank Kevin Bundy for generously sharing his K-band photometry and Christy Tremonti for making her measurements available. We are grateful to Stephane Arnout and Olivier Ilbert for making their photo-z code available for use in estimating galaxy stellar mass and are thankful to Olivier Ilbert and C.J. Ma for help in installing and implementing Le Phare. Finally, we would like to thank Charlie Conroy, Christy Tremonti, Kristian Finlator, Len Cowie, David Rupke, Dave Sanders, Chiaki Kobayashi, Ezequiel Treister and TC (the player) for useful discussion. We acknowledge the cultural significance Mauna Kea has for the Hawaiian community and with all due respect say mahalo for its use in this work.

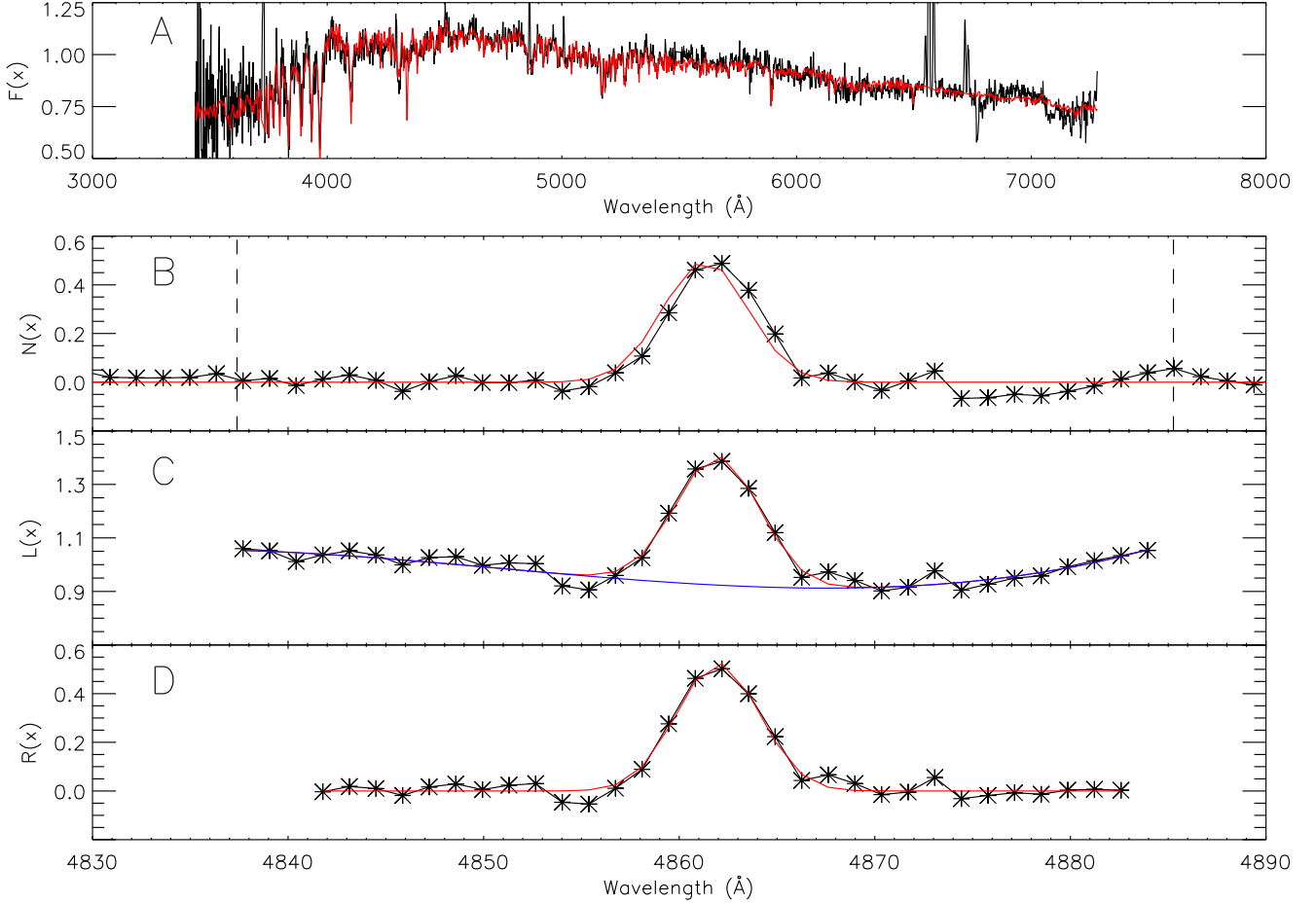


FIG. 14.— The four panels illustrate the sequence of our fitting scheme for emission lines. Panel A shows the flux vector of a typical spectra, $F(x)$, plotted against the wavelength vector, x , corresponding to each resolution element. The red line is a fit of the continuum, $C(x)$, to the spectra. In panel B $N(x)$ is the flux, $F(x)$, normalized to the global continuum, $C(x)$. A three parameter gaussian fit is overplotted in red. The dashed lines show the $\pm 10\sigma_e$ of line center, x_e , for determining the local flux. Panel C shows the local flux, $L(x)$. The blue curve is a 6-degree polynomial, $p(x)$, modeling the underlying local continuum. The red curve is a gaussian modeling the emission line. $R(x)$, panel D, is the local flux, $L(x)$, normalized to the local continuum, $p(x)$. The red curve is the fitted gaussian from which the pseudo-flux of the line is calculated. We subtract the fitted gaussian from $R(x)$ and take the rms of the data to be the noise in the continuum, σ_e .

APPENDIX

Line fitting and line ratio determination

Conventionally, when spectra are not flux calibrated, as is the case in most spectroscopic redshift surveys, equivalent widths are utilized in determining the emission line ratios used for inferring metallicity (Kobulnicky & Phillips 2003, hereafter KP03). The essential feature of equivalent widths is the normalization of the line emission to the underlying continuum. In practice the determination of equivalent width is generally an interactive process where the user is asked to input the upper and lower wavelength limits of the continuum surrounding the emission line. This process can be tedious and has the unfortunate feature of not being reproducible, varying by as much as 20% depending on the inputted wavelength limits. Here we will discuss a new automated algorithm developed to determine line ratios in a self-consistent manner.

We define $F(x)$ as the flux vector of our spectra with x being the rest-frame wavelength vector corresponding to each resolution element (panel A figure 14). We mask out $\pm 5\sigma_v$ of our rest-frame line center wavelengths (from NIST⁴) and fit a global continuum (red curve, panel A figure 14). When the velocity dispersion is not available, we make an initial estimate of σ_v by assuming a typical velocity dispersion of 150 km/s. We model the global continuum as

$$C(x) = \sum_{i=1}^{39} c_i T_i(x) + \sum_{j=0}^2 p_j x^j \quad (1)$$

where $T_i(x)$ are model stellar spectra obtained from Bruzual & Charlot (2003). We perform a bounded value non-linear

⁴ National Institute of Standards and Technologies

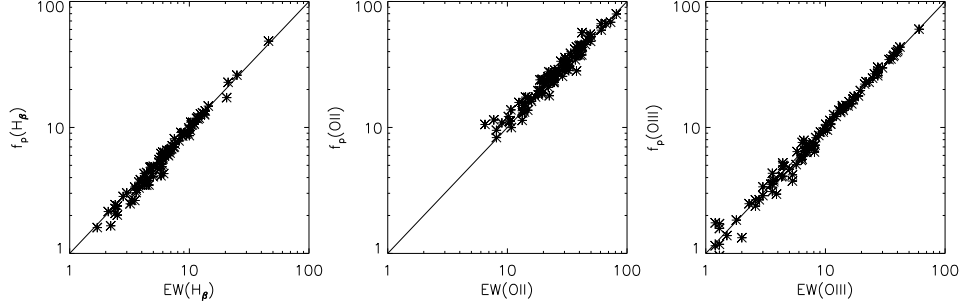


FIG. 15.— Comparison of fitted emission-line pseudo-fluxes (vertical axis) to the reported equivalent widths (horizontal axis) for 102 galaxies from the Nearby Field Galaxies Survey (Jansen et al. 2000). From left to right the plots show the H_β , [OII] and [OIII] comparisons respectively. The solid line in each plot shows the one-to-one agreement.

least square fit using the MPFIT⁵ set of routines (Markwardt 2009) in IDL to obtain c_i and p_j with the constraint that $c_i \geq 0$. We obtain a continuum-normalized flux, $N(x)$ (panel B figure 14), such that

$$N(x) = \frac{F(x)}{C(x)} - 1, \quad (2)$$

and fit a three parameter gaussian, $A_N e^{-\frac{(x-x_N)^2}{2\sigma_N^2}}$ to all emission lines of interest for metallicity. A_N , x_N and σ_N are the gain, line center and sigma of the gaussian and are used as initial estimates for fits to the local flux.

We define $L(x)$ as the local flux for each line (panel C figure 14). $L(x) = F(x)$ in the range $x_N - 10\sigma_N < x < x_N + 10\sigma_N$ (dashed lines, panel B figure 14) and zero elsewhere. We perform a bounded value non-linear least square fit to the local flux $L(x)$ with a two component model $r(x)$, such that $r(x) = p(x) + g(x)$ where

$$p(x) = \sum_{j=0}^6 b_j x^j \quad (3)$$

is a 6-degree polynomial that models the underlying continuum (blue curve, panel C figure 14) and

$$g(x) = \sum_{i=1}^n a_i e^{-\frac{(x-x_{oi})^2}{2\sigma^2}} \quad (4)$$

is a gaussian that models the emission line (red curve, panel C figure 14), where a_L , x_{oL} and σ_L are defined as the gain, center and sigma of the gaussian fit, $g(x)$, to $L(x)$ respectively. The determined pseudo-flux is not highly sensitive to the degree of polynomial fitted, but we find that a 6-degree polynomial minimizes the residuals between our measured pseudo-flux and reported equivalent widths of our comparison sample discussed below. It should be noted that σ in equation 4 does not have a summation index. If $n > 1$ then the multiple gaussians simultaneously fitted will have different a_L and x_{oL} but the same σ_L . The parameters of the gaussian are constrained such that $a_L \geq 0$, x_{oL} can only vary by $\pm 2\text{\AA}$ from the line centers obtained from NIST⁶ and $0 < \sigma_L < 10\text{\AA}$. For the [OII] $\lambda\lambda 3726, 3728$ doublet $n=2$ and for all other lines $n=1$. This enables us to fit the local continuum, $p(x)$, to all lines separately, except in the case of the [OII] doublet where we fit the continuum to both lines simultaneously.

We obtain a continuum-normalized local flux, $R(x)$ (panel D figure 14), such that

$$R(x) = \frac{L(x)}{p(x)} - 1. \quad (5)$$

We refit a model, $g_R(x)$, of the form given in equation 4 with $n=3$ for the H_β and [OIII] $\lambda\lambda 4958, 5007$ lines and $n=2$ for the [OII] $\lambda\lambda 3726, 3728$ doublet. These values of n for the two sets of lines ensures that the fitted σ will be the same for all lines in the set. We obtain a pseudo-flux for each line, f_p , such that $f_p = a_R \sigma_R \sqrt{2\pi}$, where a_R and σ_R are parameters from the fit of $g_R(x)$ to $R(x)$. We obtain an estimate of the noise in the normalized local continuum, σ_e , by taking the standard deviation of $E(x)$, where

$$E(x) = R(x) - g_R(x) = \frac{L(x) - g(x)}{p(x)} - 1. \quad (6)$$

$E(x)$ is the emission line subtracted continuum-normalized local flux. From this we determine a S/N for each line, a_R/σ_e .

⁵ <http://purl.com/net/mpfit>

⁶ This is done to account for possible errors in the redshift determination, reported line centers from NIST and/or wavelength calibrations

TABLE 1
RMS DEVIATION FROM ONE-TO-ONE AGREEMENT

| | $[OII]/H_{\beta}$ (dex) | $[OIII]/H_{\beta}$ (dex) | O_{32} (dex) | R_{23} (dex) |
|------|----------------------------|-----------------------------|-------------------|-------------------|
| KP03 | 0.11 | 0.05 | 0.12 | 0.08 |
| HJZ | 0.10 | 0.06 | 0.12 | 0.08 |

NOTE. — RMS deviation comparison of one-to-one agreement from Kobulnicky & Phillips (2003) (top row) and our automated method (bottom row).

It becomes problematic to measure an equivalent width or pseudo-flux when the S/N is low in the underlying continuum. In this situation, the continuum is poorly measured and therefore a normalization to the continuum is prone to large errors. Before normalizing the local flux, $L(x)$, to the continuum, $p(x)$, we estimate the noise of the local continuum, σ_u , by taking the rms of $U(x)$, where $U(x) = L(x) - r(x)$. We estimate the error on the mean of the continuum as σ_u/\sqrt{N} , where N is the number of data points used to calculate the mean. We calculate the mean value, \bar{p} , of the continuum fit, $p(x)$, in the region of the line, $x_o - 3\sigma < x < x_o + 3\sigma$. We determine a significance of detection for the continuum, s , such that $s = \frac{\bar{p}}{\sigma_u}$. If $s < 1$ we do not normalize to the continuum but instead fit a function of the form given in equation 4 to $D(x)$, where $D(x) = L(x) - p(x)$. We then calculate a pseudo-flux from the parameters of the fit. In this study a small fraction ($\sim 1\%$) of our objects have such low S/N in the continuum and are excluded from the study.

Comparison of line ratio determination

In order to test the robustness of our fitting method, we compare our pseudo-flux and line ratios with published equivalent widths and line ratios determined from calibrated fluxes from the Nearby Field Galaxies Survey (NFGS) (Jansen et al. 2000). KP03 compare how well interactively determined equivalent width ratios correspond to those determined from measured fluxes. We deredden the fluxes from NFGS sample as described in KP03 and use their results as a benchmark for comparison. Of the 198 galaxies in the survey, 118 have published fluxes. Of those 118, 104 galaxies have a S/N of at least 8 for $[OII]$ $\lambda\lambda$ 3726, 3728, $[OIII]$ $\lambda\lambda$ 4958, 5007 and H_{β} emission lines. We remove two additional galaxies that have a good fit determined visually but poor agreement with ratios determined from calibrated fluxes, presumably due to the underlying continuum which is poorly measured, leaving us with a sample of 102 galaxies plotted in figures 15 and 16.

Figure 15 shows a direct comparison between the the equivalent widths determined by Jansen et al. (2000) and the pseudo-flux determined by our automated method. The rms dispersion from one-to-one agreement is 0.6, 4.0 and 0.7 Å

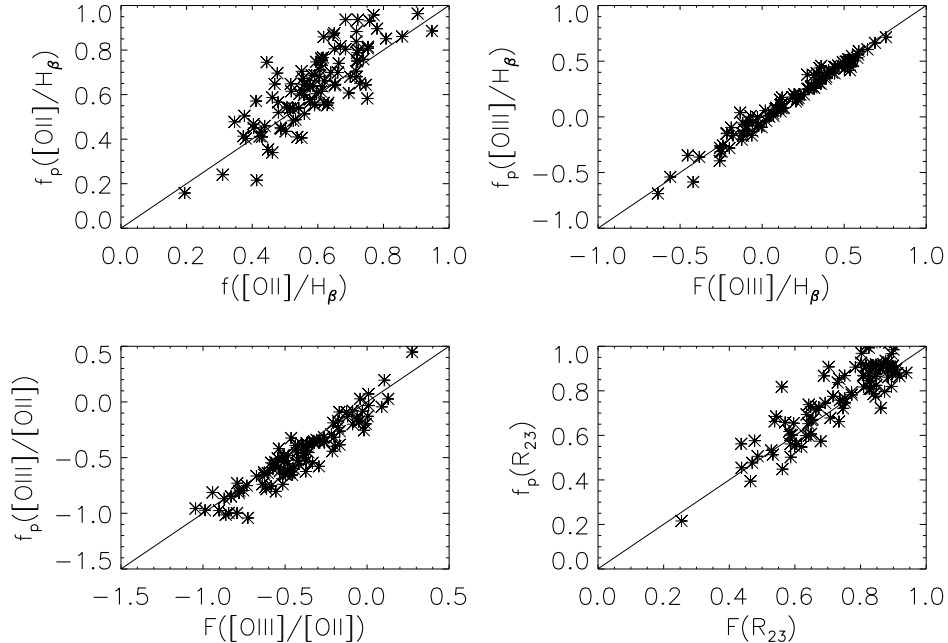


FIG. 16.— Comparison of fitted emission-line pseudo-flux ratios (vertical axis) to dereddened emission-line flux ratios (horizontal axis) for 102 galaxies from the Nearby Field Galaxies Survey (Jansen et al. 2000). From top right panel going clockwise we show the $[OII]/H_{\beta}$, $[OIII]/H_{\beta}$, R_{23} and O_{32} ratios respectively. The solid line in each panel shows the one-to-one agreement between the two methods.

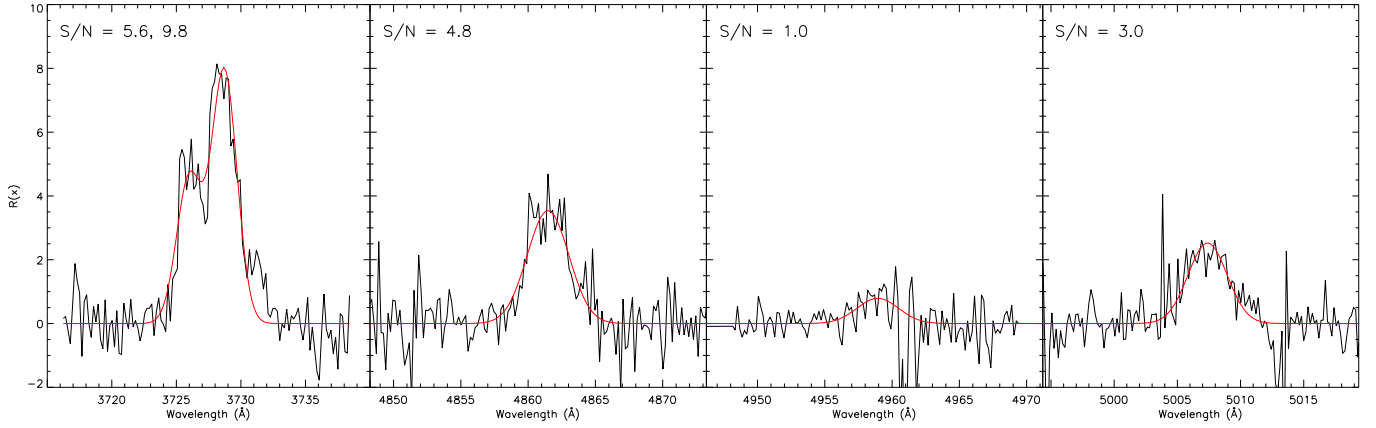


FIG. 17.— These spectra from the DEEP2 survey show the limit of the S/N for our selection criteria ($S/N \geq 3$ for H_β). From left to right, the spectra (black curve) and gaussian fit (red curve) for [OII] $\lambda\lambda 3726, 3728$, H_β , [OIII] $\lambda 4958$ and [OIII] $\lambda 5007$. The S/N for each spectrum is displayed.

with the mean value of the equivalent width being 7.5, 28.0 and 15.3 Å for H_β , [OII] and [OIII] respectively.

In order to justify the pseudo-flux can be used in inferring gas-phase metallicities, we need to establish agreement between the calibrated flux ratios and our pseudo-flux ratios. Figure 16 shows agreement in line ratios determined with our method as compared to those from calibrated fluxes with a rms dispersion from one-to-one agreement of 0.10, 0.06, 0.11 and 0.08 dex for the $[OII]/H_\beta$, $[OIII]/H_\beta$, O_{32} and R_{23} ratios respectively. Table 1 gives the rms deviation from one-to-one agreement between line ratios determined using the two different methods. The top row shows the rms deviation from KP03 and the bottom row shows the rms deviation for our automated method for our sample of 102 galaxies. In this local sample the errors from the statistical measurement uncertainties are about one half of those introduced by using equivalent widths or our pseudo-flux in line ratio determinations. Because galaxies are fainter at higher redshift, we expect them to have larger measurement uncertainties, thereby making the errors from using equivalent widths comparable or even less than the statistical measurement uncertainties.

The O_{32} and R_{23} ratios are of particular importance because of their use in inferring metallicities. Figure 16 and Table 1 demonstrate that our automated method for determining line ratios are comparable to those that employ an interactive determination of equivalent widths. However, our automated method has several advantages over interactive determination of equivalent widths. 1) The method is automated so considerably faster than interactively determining equivalent widths and much more practical when working with large samples. 2) The automated method yields results that are reproducible because it no longer requires the input of wavelength limits in determining equivalent widths. 3) The measurement errors in flux, when available, can be propagated through to the determination of metallicity and therefore provide a much more robust estimate of the true errors in $12 + \log[O/H]$. 4) In data where a low S/N makes it difficult to distinguish between the line and the continuum, the automatic fit is less susceptible to confusion (see figure 17). 5) Low S/N spectra where the continuum is not detected, equivalent widths cannot be determined. These cases are handled in a much more robust manner allowing us to measure a pseudo-flux even when equivalent widths cannot be measured.

REFERENCES

- Arnouts, S., et al. 2005, *ApJ*, 619, L43
 Bell, E. F., McIntosh, D. H., Katz, N., & Weinberg, M. D. 2003, *ApJS*, 149, 289
 Bessell, M. S. 1990, *PASP*, 102, 1181
 Bonnell, I. A., Larson, R. B., & Zinnecker, H. 2007, *Protostars and Planets V*, 149
 Bouché, N., et al. 2007, *ApJ*, 671, 303
 Brooks, A. M., Governato, F., Booth, C. M., Willman, B., Gardner, J. P., Wadsley, J., Stinson, G., & Quinn, T. 2007, *ApJ*, 655, L17
 Bruzual, G., & Charlot, S. 2003, *MNRAS*, 344, 1000
 Bundy, K., et al. 2006, *ApJ*, 651, 120
 Calura, F., Pipino, A., Chiappini, C., Matteucci, F., & Maiolino, R. 2009, *A&A*, 504, 373
 Calzetti, D., Armus, L., Bohlin, R. C., Kinney, A. L., Koornneef, J., & Storchi-Bergmann, T. 2000, *ApJ*, 533, 682
 Caputi, K. I., et al. 2009, *ApJ*, 707, 1387
 Carollo, C. M., & Lilly, S. J. 2001, *ApJ*, 548, L153
 Chabrier, G. 2003, *PASP*, 115, 763
 Charlot, S., & Longhetti, M. 2001, *MNRAS*, 323, 887
 Coil, A. L., Newman, J. A., Kaiser, N., Davis, M., Ma, C.-P., Kocevski, D. D., & Koo, D. C. 2004, *ApJ*, 617, 765
 Conroy, C., Gunn, J. E., & White, M. 2009, *ApJ*, 699, 486
 Cowie, L. L., & Barger, A. J. 2008, *ApJ*, 686, 72
 Cowie, L. L., Songaila, A., Hu, E. M., & Cohen, J. G. 1996, *AJ*, 112, 839
 Daddi, E., et al. 2009, *ArXiv e-prints*
 Dalcanton, J. J. 2007, *ApJ*, 658, 941
 Dalcanton, J. J., Yoachim, P., & Bernstein, R. A. 2004, *ApJ*, 608, 189
 Davis, M., et al. 2003, in *Society of Photo-Optical Instrumentation Engineers (SPIE) Conference Series*, Vol. 4834, *Society of Photo-Optical Instrumentation Engineers (SPIE) Conference Series*, ed. P. Guhathakurta, 161–172
 de Rossi, M. E., Tissera, P. B., & Scannapieco, C. 2007, *MNRAS*, 374, 323
 Dekel, A., & Silk, J. 1986, *ApJ*, 303, 39
 Drory, N., Bender, R., & Hopp, U. 2004, *ApJ*, 616, L103
 Edmunds, M. G. 1990, *MNRAS*, 246, 678
 Elmegreen, B. G. 2009, in *The Evolving ISM in the Milky Way and Nearby Galaxies*
 Erb, D. K. 2008, *ApJ*, 674, 151
 Erb, D. K., Shapley, A. E., Pettini, M., Steidel, C. C., Reddy, N. A., & Adelberger, K. L. 2006, *ApJ*, 644, 813

- Faber, S. M., et al. 2003, in Society of Photo-Optical Instrumentation Engineers (SPIE) Conference Series, Vol. 4841, Society of Photo-Optical Instrumentation Engineers (SPIE) Conference Series, ed. M. Iye & A. F. M. Moorwood, 1657–1669
- Faber, S. M., et al. 2007, *ApJ*, 665, 265
- Ferland, G. J. 1996, *Hazy, A Brief Introduction to Cloudy 90*, ed. G. J. Ferland
- Feulner, G., Gabasch, A., Salvato, M., Drory, N., Hopp, U., & Bender, R. 2005, *ApJ*, 633, L9
- Finlator, K., & Davé, R. 2008, *MNRAS*, 385, 2181
- Fontana, A., et al. 2004, *A&A*, 424, 23
- Franceschini, A., et al. 2006, *A&A*, 453, 397
- Garnett, D. R. 2002, *ApJ*, 581, 1019
- Garnett, D. R., Shields, G. A., Skillman, E. D., Sagan, S. P., & Dufour, R. J. 1997, *ApJ*, 489, 63
- Genel, S., et al. 2008, *ApJ*, 688, 789
- Hopkins, A. M., & Beacom, J. F. 2006, *ApJ*, 651, 142
- Hooversten, E. A., & Glazebrook, K. 2008, *ApJ*, 675, 163
- Ilbert, O., et al. 2006, *A&A*, 453, 809
- . 2009, *ArXiv e-prints*
- Impey, C., & Bothun, G. 1997, *ARA&A*, 35, 267
- Jansen, R. A., Fabricant, D., Franx, M., & Caldwell, N. 2000, *ApJS*, 126, 331
- Juneau, S., et al. 2005, *ApJ*, 619, L135
- Kannappan, S. J. 2004, *ApJ*, 611, L89
- Kauffmann, G., & Charlot, S. 1998, *MNRAS*, 294, 705
- Kennicutt, Jr., R. C. 1998, *ApJ*, 498, 541
- Kewley, L. J., & Dopita, M. A. 2002, *ApJS*, 142, 35
- Kewley, L. J., & Ellison, S. L. 2008, *ApJ*, 681, 1183
- Kobayashi, C., Springel, V., & White, S. D. M. 2007, *MNRAS*, 376, 1465
- Kobulnicky, H. A., Kennicutt, Jr., R. C., & Pizagno, J. L. 1999, *ApJ*, 514, 544
- Kobulnicky, H. A., & Kewley, L. J. 2004, *ApJ*, 617, 240
- Kobulnicky, H. A., & Koo, D. C. 2000, *ApJ*, 545, 712
- Kobulnicky, H. A., & Phillips, A. C. 2003, *ApJ*, 599, 1031
- Kobulnicky, H. A., et al. 2003, *ApJ*, 599, 1006
- Köppen, J., Weidner, C., & Kroupa, P. 2007, *MNRAS*, 375, 673
- Kroupa, P. 2001, *MNRAS*, 322, 231
- Lada, C. J., & Lada, E. A. 2003, *ARA&A*, 41, 57
- Lamareille, F., et al. 2009, *A&A*, 495, 53
- Lamareille, F., Mouhcine, M., Contini, T., Lewis, I., & Maddox, S. 2004, *MNRAS*, 350, 396
- Larson, R. B. 1974, *MNRAS*, 169, 229
- Larson, R. B., & Dinerstein, H. L. 1975, *PASP*, 87, 911
- Le Floc'h, E., et al. 2005, *ApJ*, 632, 169
- Lequeux, J., Peimbert, M., Rayo, J. F., Serrano, A., & Torres-Peimbert, S. 1979, *A&A*, 80, 155
- Liang, Y. C., et al. 2009, *ArXiv e-prints*
- Maier, C., Lilly, S. J., Carollo, C. M., Stockton, A., & Brodwin, M. 2005, *ApJ*, 634, 849
- Maier, C., Meisenheimer, K., & Hippelein, H. 2004, *A&A*, 418, 475
- Maiolino, R., et al. 2008, *A&A*, 488, 463
- Mannucci, F., et al. 2009, *MNRAS*, 398, 1915
- Markwardt, C. B. 2009, *ArXiv e-prints*
- Matteucci, F. 1994, *A&A*, 288, 57
- McGaugh, S. S., & de Blok, W. J. G. 1997, *ApJ*, 481, 689
- Meurer, G. R., et al. 2009, *ApJ*, 695, 765
- Mouchine, M., Gibson, B. K., Renda, A., & Kawata, D. 2008, *ArXiv e-prints*
- Muñoz-Mateos, J. C., Gil de Paz, A., Boissier, S., Zamorano, J., Jarrett, T., Gallego, J., & Madore, B. F. 2007, *ApJ*, 658, 1006
- Neistein, E., van den Bosch, F. C., & Dekel, A. 2006, *MNRAS*, 372, 933
- Oppenheimer, B. D., & Davé, R. 2008, *MNRAS*, 387, 577
- Osterbrock, D. E. 1989, *Astrophysics of gaseous nebulae and active galactic nuclei*, ed. D. E. Osterbrock
- Pagel, B. E. J. 1997, *Nucleosynthesis and Chemical Evolution of Galaxies*, ed. Pagel, B. E. J.
- Pagel, B. E. J., Edmunds, M. G., Blackwell, D. E., Chun, M. S., & Smith, G. 1979, *MNRAS*, 189, 95
- Pérez-González, P. G., et al. 2008, *ApJ*, 675, 234
- Pettini, M., Shapley, A. E., Steidel, C. C., Cuby, J.-G., Dickinson, M., Moorwood, A. F. M., Adelberger, K. L., & Giavalisco, M. 2001, *ApJ*, 554, 981
- Reddy, N. A., Steidel, C. C., Pettini, M., Adelberger, K. L., Shapley, A. E., Erb, D. K., & Dickinson, M. 2008, *ApJS*, 175, 48
- Salpeter, E. E. 1955, *ApJ*, 121, 161
- Salzer, J. J., Lee, J. C., Melbourne, J., Hinz, J. L., Alonso-Herrero, A., & Jangren, A. 2005, *ApJ*, 624, 661
- Savaglio, S., et al. 2005, *ApJ*, 635, 260
- Schechter, P. 1976, *ApJ*, 203, 297
- Schlegel, D. J., Finkbeiner, D. P., & Davis, M. 1998, *ApJ*, 500, 525
- Schmidt, M. 1959, *ApJ*, 129, 243
- . 1963, *ApJ*, 137, 758
- Searle, L., & Sargent, W. L. W. 1972, *ApJ*, 173, 25
- Shapley, A. E., Coil, A. L., Ma, C.-P., & Bundy, K. 2005, *ApJ*, 635, 1006
- Shapley, A. E., Erb, D. K., Pettini, M., Steidel, C. C., & Adelberger, K. L. 2004, *ApJ*, 612, 108
- Skillman, E. D., Kennicutt, R. C., & Hodge, P. W. 1989, *ApJ*, 347, 875
- Somerville, R. S., & Primack, J. R. 1999, *MNRAS*, 310, 1087
- Springel, V., & Hernquist, L. 2003, *MNRAS*, 339, 289
- Tacconi, L. J., et al. 2010, *Nature*, 463, 781
- Tassis, K., Kravtsov, A. V., & Gnedin, N. Y. 2008, *ApJ*, 672, 888
- Tissera, P. B., De Rossi, M. E., & Scannapieco, C. 2005, *MNRAS*, 364, L38
- Tremonti, C. A., et al. 2004, *ApJ*, 613, 898
- van den Bergh, S. 1962, *AJ*, 67, 486
- van Dokkum, P. G. 2008, *ApJ*, 674, 29
- Weidner, C., & Kroupa, P. 2005, *ApJ*, 625, 754
- Willmer, C. N. A., et al. 2006, *ApJ*, 647, 853
- Zaritsky, D., Kennicutt, Jr., R. C., & Huchra, J. P. 1994, *ApJ*, 420, 87
- Zhong, G. H., Liang, Y. C., Liu, F. S., Hammer, F., Hu, J. Y., Chen, X. Y., Deng, L. C., & Zhang, B. 2008, *MNRAS*, 391, 986